AGU PUBLICATIONS

JGR

Journal of Geophysical Research: Solid Earth

RESEARCH ARTICLE
10.1002/2017JB014495

Investigation of Backprojection Uncertainties With *M6* Earthquakes

Wenyuan Fan[1] **and Peter M. Shearer**[1]

[1] Scripps Institution of Oceanography, University of California, San Diego, CA, USA

Key Points:
- Backprojection empirical time corrections are valid up to 700 km with median spatial imaging uncertainties of 25 km
- Incoherence of backprojection images because of 3-D structure does not grow with epicentral distance
- Empirical observations suggest it is challenging to improve backprojection images with aftershock calibrations

Supporting Information:
- Supporting Information S1

Correspondence to:
W. Fan
w3fan@ucsd.edu

Citation:
Fan, W., & Shearer, P. M. (2017). Investigation of backprojection uncertainties with *M6* earthquakes. *Journal of Geophysical Research: Solid Earth*, *122*. https://doi.org/10.1002/2017JB014495

Received 30 MAY 2017
Accepted 2 SEP 2017
Accepted article online 12 SEP 2017

Abstract We investigate possible biasing effects of inaccurate timing corrections on teleseismic *P* wave backprojection imaging of large earthquake ruptures. These errors occur because empirically estimated time shifts based on aligning *P* wave first arrivals are exact only at the hypocenter and provide approximate corrections for other parts of the rupture. Using the Japan subduction zone as a test region, we analyze 46 *M6*–*M7* earthquakes over a 10 year period, including many aftershocks of the 2011 *M9* Tohoku earthquake, performing waveform cross correlation of their initial *P* wave arrivals to obtain hypocenter timing corrections to global seismic stations. We then compare backprojection images for each earthquake using its own timing corrections with those obtained using the time corrections from other earthquakes. This provides a measure of how well subevents can be resolved with backprojection of a large rupture as a function of distance from the hypocenter. Our results show that backprojection is generally very robust and that the median subevent location error is about 25 km across the entire study region (~700 km). The backprojection coherence loss and location errors do not noticeably converge to zero even when the event pairs are very close (<20 km). This indicates that most of the timing differences are due to 3-D structure close to each of the hypocenter regions, which limits the effectiveness of attempts to refine backprojection images using aftershock calibration, at least in this region.

1. Introduction

Backprojection is one of the primary tools to investigate large earthquake rupture propagation without requiring many prior assumptions about fault geometry or rupture speed. Ever since its first application to the 2004 Sumatra-Andaman earthquake (Ishii et al., 2005), backprojection has proven useful in studying complex earthquake ruptures, early aftershock detection, and hazard early warning (e.g., Allmann & Shearer, 2007; An & Meng, 2016; Fan & Shearer, 2016a; Kiser & Ishii, 2011, 2012; Koper et al., 2011; Meng et al., 2011; Nissen et al., 2016; Okuwaki et al., 2014; Walker et al., 2005; Wang et al., 2012; Yagi et al., 2012). Backprojection images, in conjunction with rupture dynamics simulations and knowledge of local tectonics, have led to improved understanding of earthquake physics and subduction zone stress transfer patterns (e.g., Fan et al., 2016; Huang et al., 2012, 2014).

Backprojection takes advantage of source-receiver reciprocity. It assumes that teleseismic *P* waves provide relatively undistorted records of seismic radiation, such that differences in source locations on the fault can be approximated as time shifts in the records. This permits stacking methods to be used to extract coherent signals to map earthquake rupture propagation, an adjoint approximation that is often more robust than formal inversion (Claerbout & Fomel, 2008). Backprojection works even with high-frequency waveforms, which can provide higher spatial and temporal resolution but are often challenging to model deterministically with current forward calculation methods and Earth structure models (e.g., Komatitsch et al., 2004; Mancinelli et al., 2016). These advantages, together with the need for few prior assumptions, make backprojection suited for resolving even very complex earthquake ruptures (e.g., Satriano et al., 2012; Walker & Shearer 2009; Wang et al., 2012).

The simplicity of backprojection helps to provide stability in its results, such that different groups often get very similar backprojection source models even when different data sets and stacking approaches are used (e.g., Fan & Shearer, 2015; Grandin et al., 2015; Wang & Mori, 2016; Yagi & Okuwaki, 2015; Zhang et al., 2016). However, the method can suffer from imaging artifacts or uncertainties because it heavily relies on the station network geometry and data quality. For example, swimming artifacts commonly appear when only using regional arrays, in which backprojection energy migrates toward the arrays because of trade-offs between

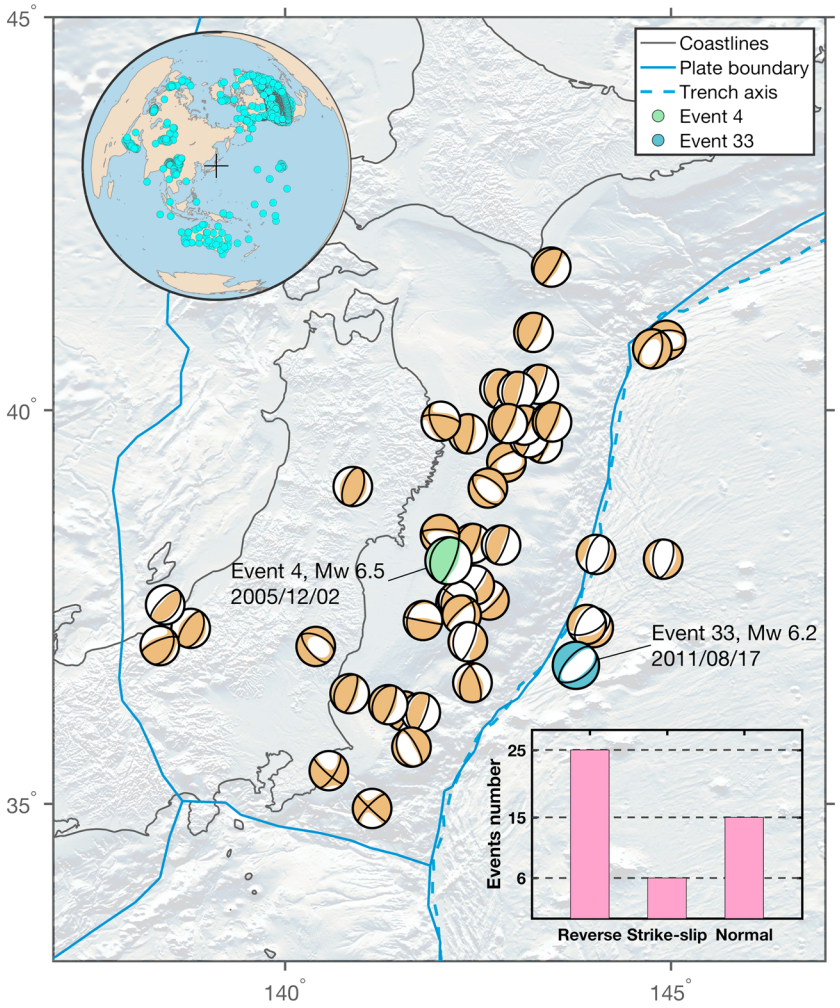

Figure 1. *M*6 earthquakes within the Japan Trench and the seismic stations used. Forty-six earthquakes (of these, 39 and 41 were investigated in the low- and high-frequency bands, respectively) with centroid depths shallower than 40 km recorded globally from 2004 to 2015 are shown with GCMT focal mechanisms (Ekström et al., 2012). The top left corner insert shows the stations used in this study. The bottom right corner insert shows the distribution of focal mechanisms (Strike-slip earthquakes are defined when the rake of both nodal planes are within 45° of 0° or 180°. Normal-/reverse-faulting earthquakes have rakes within 45° of −90°/90°).

the radiation origin time and source-receiver distance (e.g., Koper et al., 2012; Meng et al., 2012; Xu et al., 2009). In addition, apparent source offsets may appear in regional array backprojection images due to neglecting depth variations in radiation. Understanding backprojection resolution and uncertainty is important because biased backprojection source models may cause erroneous interpretations of rupture physics (e.g., Ishii et al., 2007; Koper et al., 2012; Meng et al., 2016; Walker & Shearer, 2009). However, assessing the uncertainties is challenging because backprojection relies on waveform stacking instead of optimizing a misfit function. Examples of methods used to measure backprojection resolution and uncertainty include (1) using synthetic tests to estimate resolution kernels and the effect of depth phases, (2) seismogram resampling tests to assess the statistical significance of features, and (3) backprojection of smaller events near the main shock of interest to provide empirical measures of image resolution (e.g., Fan & Shearer, 2016b; Fan et al., 2016). However, none of these approaches addresses model-related uncertainties, i.e., how much bias in backprojection images is caused by inaccuracies in the assumed source-receiver Green's functions. Here we focus on the specific issue as to whether the empirical timing corrections obtained from the initial *P* wave alignment for the epicenter are applicable to other parts of the fault.

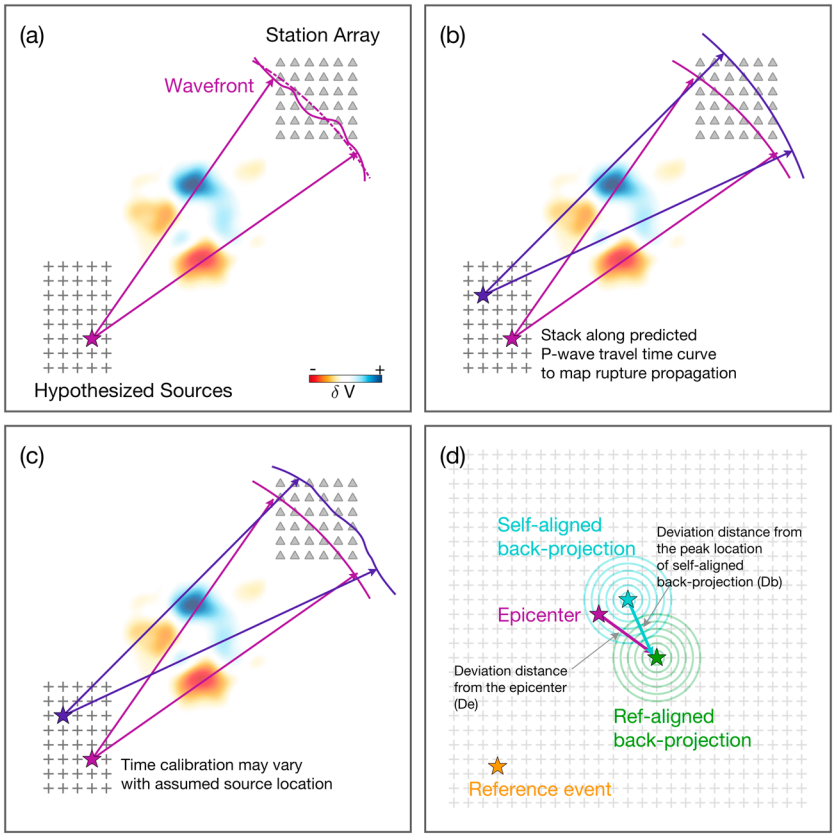

Figure 2. A cartoon illustrating the backprojection method and the biasing effect of 3-D structure on travel times. (a) Travel times from the hypocenter (star) are perturbed by 3-D structure, such that the wavefront at the stations (wiggly solid line) is distorted compared to that predicted by a 1-D model (dashed line). However, by cross correlating and aligning the first-arriving *P* waves from the hypocenter, time correction factors can be applied to bring the arrival times into agreement with theoretical predictions. (b) Backprojection imaging stacks the seismograms for each source grid point using theoretical differential times relative to a source at the epicenter. (c) However, the time corrections computed for the hypocenter are not necessarily correct for other source points because the rays travel through different 3-D structure, and thus, the backprojection images may be biased. (d) Using cross-correlation results from pairs of earthquakes, we test to see how much this bias will shift the backprojection images of target earthquakes, as measured by the distance of the image peak from the epicenter (De) or the backprojection image with self-aligned time calibrations (Db).

At the relatively high-frequencies used in backprojection, time shifts due to 3-D structure along the ray paths will prevent coherent stacking of the records if only a 1-D model is assumed. Because 3-D tomographic models do not yet have the resolution to predict these time shifts, the standard approach for estimating them is to align the first-arriving waves from the hypocenter using waveform cross correlation. These empirical time shifts are then used to correct the times for all the hypothetical source locations in the backprojection calculation. However, the timing corrections are only exact at the hypocenter and presumably can become increasingly inaccurate at more distant locations on the fault, where the rays will traverse different parts of the underlying 3-D velocity structure. This will cause the backprojection stacks to be less coherent at these locations, reducing the apparent amplitudes of features. Perhaps more seriously, inaccurate time corrections might bias the locations of subevents away from their true locations.

One way to address the timing correction issue is to use records from other earthquakes within the main shock rupture region (often aftershocks of the main shock) as calibration events to obtain more accurate time shifts at varying locations on or near the fault (Ishii et al., 2007). This idea has been explored by applying waveform cross correlation of these aftershocks to extract empirical time corrections for the regions close to the aftershocks (e.g., Ishii et al., 2007; Meng et al., 2016). For the 2004 Sumatra-Andaman earthquake,

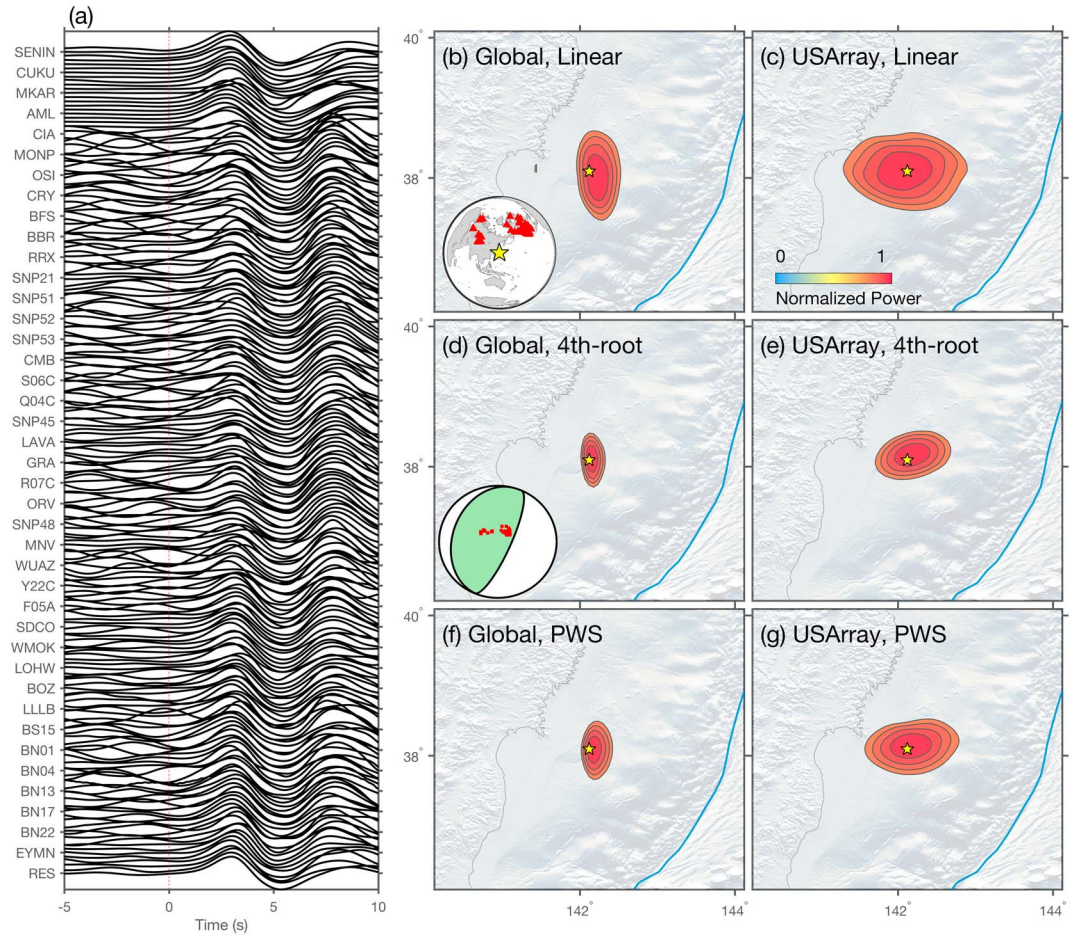

Figure 3. Backprojection results for Event 4 (Figure 1) with self-aligned time calibrations (0.05–0.3 Hz, 80% energy contour). (a) Velocity records sorted with azimuth. (b, d, and f) Integrated backprojection result of the first 20 s with linear, fourth-root stacking, and phase-weighted stacking (PWS). Station map (Figure 3b). Lower hemisphere *P* wave polarities of the stations, the focal mechanism is for Event 4 (2 December 2005 M_w6.5) (Figure 3d). (c, e, and g) Similar to Figures 3b, 3d, and 3f, but only using stations within the azimuthal range from 0° to 90°.

the aftershock-calibrated backprojection image shows more heterogeneous small-scale features compared to the smoother hypocenter-calibrated image, although the main features are very similar (Ishii et al., 2007). However, aftershocks that can be used for calibration ($M \geq 5.5$) generally do not span the entire rupture region and it is unclear how close they need to be to the backprojection source locations in order to improve the image and whether interpolation of timing corrections between aftershock locations is a valid approach.

Here we explore these issues by studying *P* wave timing corrections for 46 *M*6 earthquakes within the Japan subduction zone, including how they vary as a function of event distance and how these differences will affect backprojection images, in particular to what extent the empirical timing corrections fail when large earthquakes rupture hundreds of kilometers. By backprojecting events using the timing corrections derived from different events, we show that a single set of empirical time corrections can produce reasonably unbiased images across our entire study region (~700 km). There is loss of coherence, particularly at higher frequencies, but errors in imaged source locations are mostly less than 40 km (median about 25 km) and the errors are only a weak function of distance from the calibration event. Our results suggest that it is challenging to improve backprojection images with aftershock calibration because the region of improvement is confined to the close vicinity of each aftershock, limiting the effectiveness of interpolation of timing corrections between events,

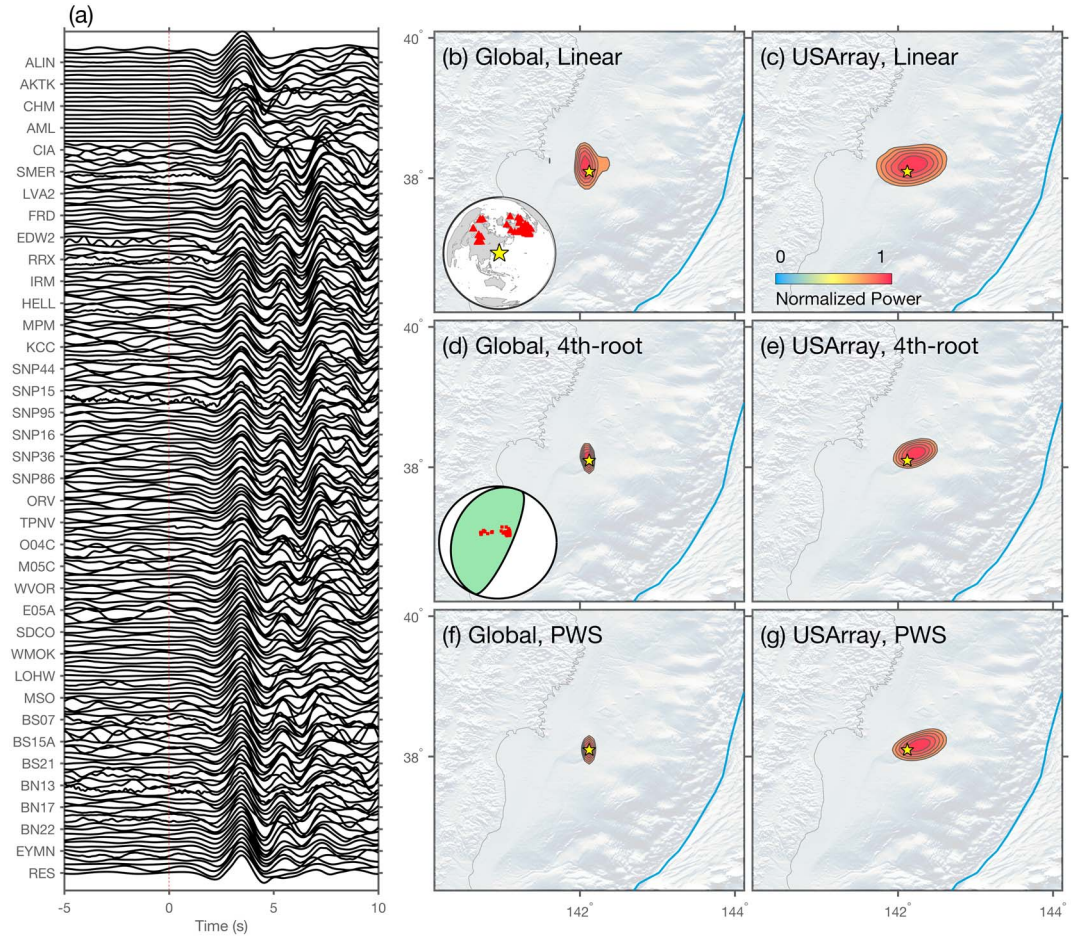

Figure 4. Backprojection results for Event 4 (Figure 1) with self-aligned time calibrations (0.3–1 Hz, 75% energy contour). Legends are the same as similar to Figure 3.

given that the aftershock coverage is typically sparse and nonuniform. Our results provide quantitative guidelines for interpreting backprojection results in the Japan trench and show that current backprojection source models are reasonably well resolved and robust.

2. Data and Method

2.1. Data

To explore backprojection uncertainties, we study moderate earthquakes ($6 \leq M_w \leq 7$) within the Japan subduction zone, which can be approximated as point sources in the far field. We select this region because of its extensive *M*6 earthquakes, particularly after the 2011 Tohoku earthquake, covering the whole area without large spatial gaps along the trench axis. The station coverage is good, with regional arrays in the United States, Europe, and Australia, in addition to the stations of the Global Seismic Network (GSN), within epicentral distances of 30° to 90° from the earthquakes, providing good azimuthal coverage for backprojection (Figure 1).

We examine 46 *M*6 earthquakes occurring during the time period from 2004 October to 2015 February with Global Centroid Moment Tensor (GCMT) centroid depths shallower than 40 km (Figure 1 and Table S1 in the supporting information) (Ekström et al., 2012). The median and average moment magnitudes of the *M*6 earthquakes are 6.2 and 6.3, and the median and average hypocenter depths are 15.5 and 17.8 km. Twenty-five of the events are reverse-faulting earthquakes, most of which occurred at the plate interface, 15 are normal-faulting earthquakes, and 6 are strike-slip earthquakes (Strike-slip earthquakes are defined when the rake of both nodal planes are within 45° of 0° or 180°. Normal-/Reverse-faulting earthquakes

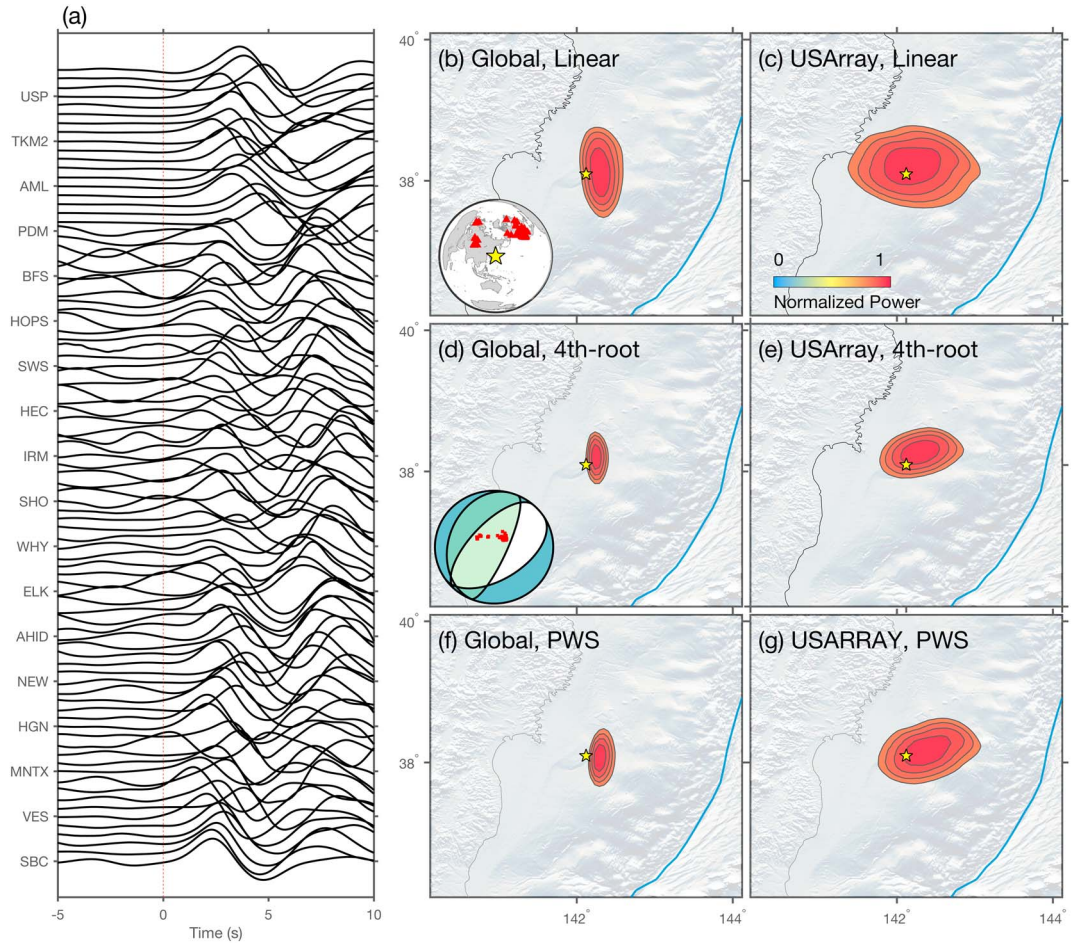

Figure 5. Backprojection results (0.05–0.3 Hz, 80% energy contour) for Event 4 with time calibrations from Event 33 (Figure 1). (a) Velocity records sorted with azimuth. (b, d, and f) Integrated backprojection result of the first 20 s with linear, fourth-root stacking, and phase-weighted stacking. Station map (Figure 5b). Lower hemisphere *P* wave polarities of the stations, the focal mechanism is the calibration event (Event 33, 17 August 2011, M_w6.2); the light green transparent focal mechanism is the target event (Event 4, 2 December 2005, M_w6.5) (Figure 5d). (c, e, and g) Similar to Figures 5b, 5d, and 5f but only using stations within the azimuthal range from 0° to 90°.

have rakes within 45° of −90°/90°, Figure 1). The seismograms used for analysis are from 2,749 globally distributed stations with 431 stations recording more than 15 earthquakes with high-quality data (Figure 1). These stations are in the 30° to 90° epicentral distance range that complex *P* waveforms introduced by mantle discontinuities and the core-mantle boundary are unlikely to be present.

The data were downloaded from the Data Management Center (DMC) of Incorporated Research Institutions for Seismology (IRIS) (Figure 1) and filtered into two frequency bands (low-frequency 0.05–0.3 Hz and high-frequency 0.3–1 Hz). Some events only had usable data in one frequency band—in total, 39 and 41 earthquakes were analyzed in the low- and high-frequency bands, respectively. For example, several aftershocks of the 2011 *M*9 Tohoku earthquake have poor quality data in the low-frequency band but have relatively clear signals in the high-frequency band. For a given earthquake, stations close to the GCMT nodal planes are removed, and only stations sharing the same GCMT *P* wave polarities are used for backprojection analysis after self-normalization. In this study, we adopt these strict quality control criteria to isolate the effects of empirical timing corrections. In practice, applying polarity changes to well-correlated records can increase the number of usable traces and improve the data coverage for large earthquakes (e.g., $M \geq 8$). All the traces are visually inspected to ensure good data quality. For our study region, we loosely define stations within 0° to 90° azimuthal range as USArray and will refer to all the usable stations, including North American stations, as the global array.

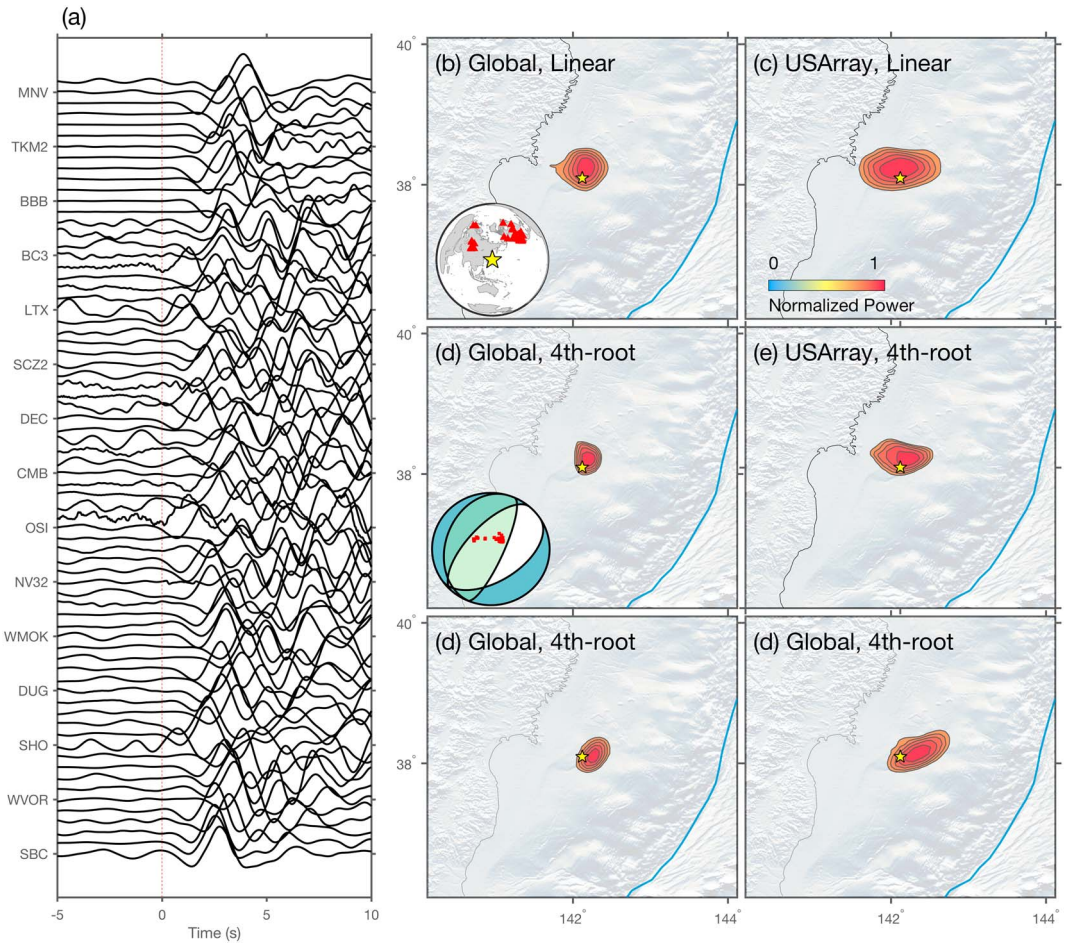

Figure 6. Backprojection results (0.3–1 Hz, 75% energy contour) for Event 4 with time calibrations from Event 33 (Figure 1). Legends are the same as similar to Figure 5.

2.2. Method

We follow closely the backprojection procedures described in Fan and Shearer (2015) to image the 46 *M*6 earthquakes. We apply a standard time domain backprojection approach, in which we empirically align the initial *P* waves, shift the records using the 1-D-model-predicted relative time offsets for different locations, and stack the shifted records to map coherent seismic radiators. Strong signals will be observed when the seismograms constructively interfere, as should occur for true sources of seismic radiation, whereas weak signals are due to destructive interference, which should occur in regions without seismic radiation. We experiment with both linear and nonlinear stacking approaches. Linear stacking retains the relative radiation strength but is more likely to suffer from artifacts due to anomalously strong signals on individual seismograms. Nonlinear stacking approaches, *N*th root stacking and phase-weighted stacking (PWS), can sharpen signals and suppress noise at the cost of absolute amplitude information (McFadden et al., 1986; Schimmel & Paulssen, 1997; Rost & Thomas, 2002; Xu et al., 2009). In this study, we focus on exploring variations in the backprojection images caused by (1) different frequency bands (low-frequency 0.05–0.3 Hz and high-frequency 0.3–1 Hz), (2) different stacking approaches (linear and nonlinear stacking), and (3) different array configurations (global and regional arrays).

In practice, we first grid potential sources at 5 km spacing across a box centered on the epicenter, spanning 200 km in latitude by 200 km in longitude. In principle, the source locations could be three dimensional, but teleseismic *P* wave data cannot resolve vertical rupture propagation for shallow earthquakes because of its poor depth sensitivity. Therefore, we consider only horizontal source grids fixed at the hypocentral depths. We compute empirical timing corrections for each event by cross correlating the first few seconds of the records

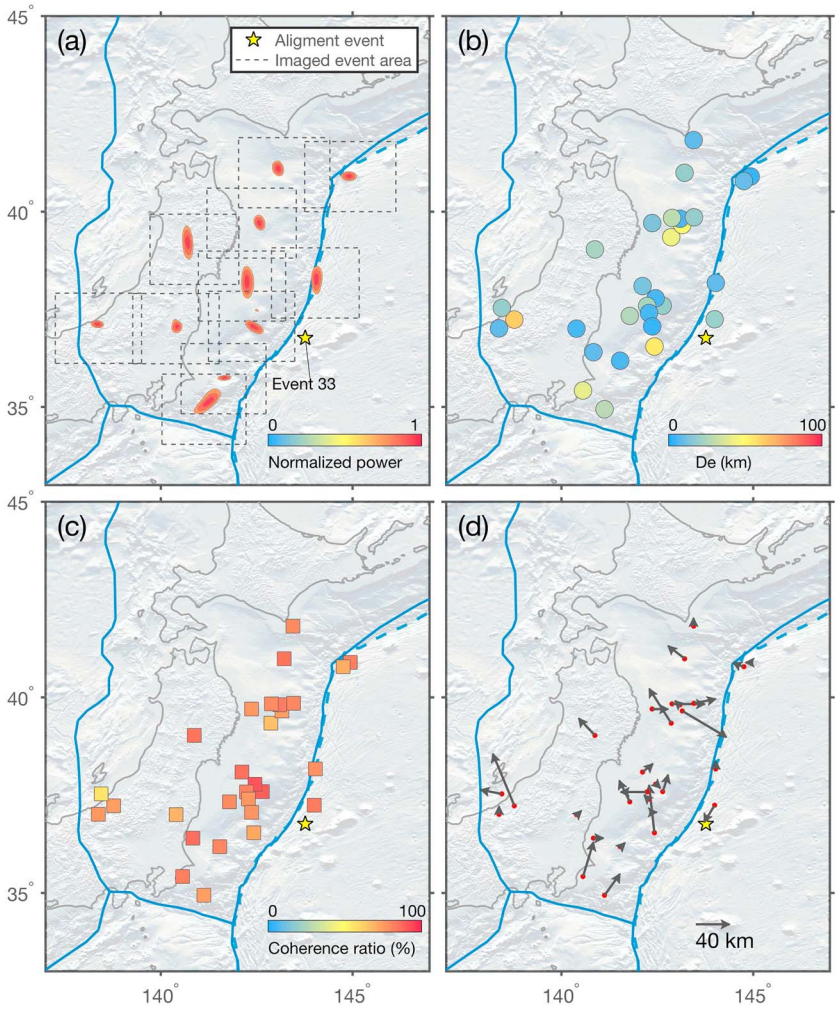

Figure 7. Backprojection results with time calibrations from reference Event 33 applied to 29 other events (Figure 1, 75% energy contour). (a) Examples of integrated backprojection images of the first 20 s. For clarity, only 11 events are shown here, the rest can be seen in Figure S1. (b) Deviation distances from the epicenters (De) for the 29 events. (c) Coherence ratio for the 29 events. (d) Deviation distance (De) and azimuth for the 29 events. For visibility, the length of the arrows is exaggerated compared to the map scale.

(~8 s for 0.05–0.3 Hz and ~5 s for 0.3–1 Hz) to empirically align the seismograms to neutralize 3-D velocity structure influences (Figure 2a) (Houser et al., 2008). In this study, we do not examine the uncertainties of the empirical timing corrections, which is a separate issue relating to waveform cross-correlation algorithms and the coherence of the waveforms (VanDecar & Crosson, 1990). Polarity flips are not allowed during cross correlation because only stations sharing the same *P* wave polarities are selected. We then shift the seismograms to stack at all the hypothetical source grids with respect to the relative time differences between the grids and the epicenter (Figure 2b). The time differences are calculated with the IASP91 1-D velocity model (Kennett & Engdahl, 1991). Both linear and nonlinear stacking are employed to explore their effects on the imaging results with $N = 4$ for Nth root stacking and $\nu = 3$ for phase-weighted stacking. During stacking, the seismograms are inversely weighted by the number of contributing stations within 5° to avoid biasing the results by a single densely instrumented region. No postsmoothing or postprocessing is applied to the backprojection images.

As an example, the 2 December 2005 M_w6.5 reverse-faulting earthquake (Event 4, Figure 1) is imaged in two frequency bands with both global stations and USArray (Figures 3 and 4). The waveforms are highly coherent for the stations in the Northern Hemisphere, whereas the Australian array data did not pass the quality

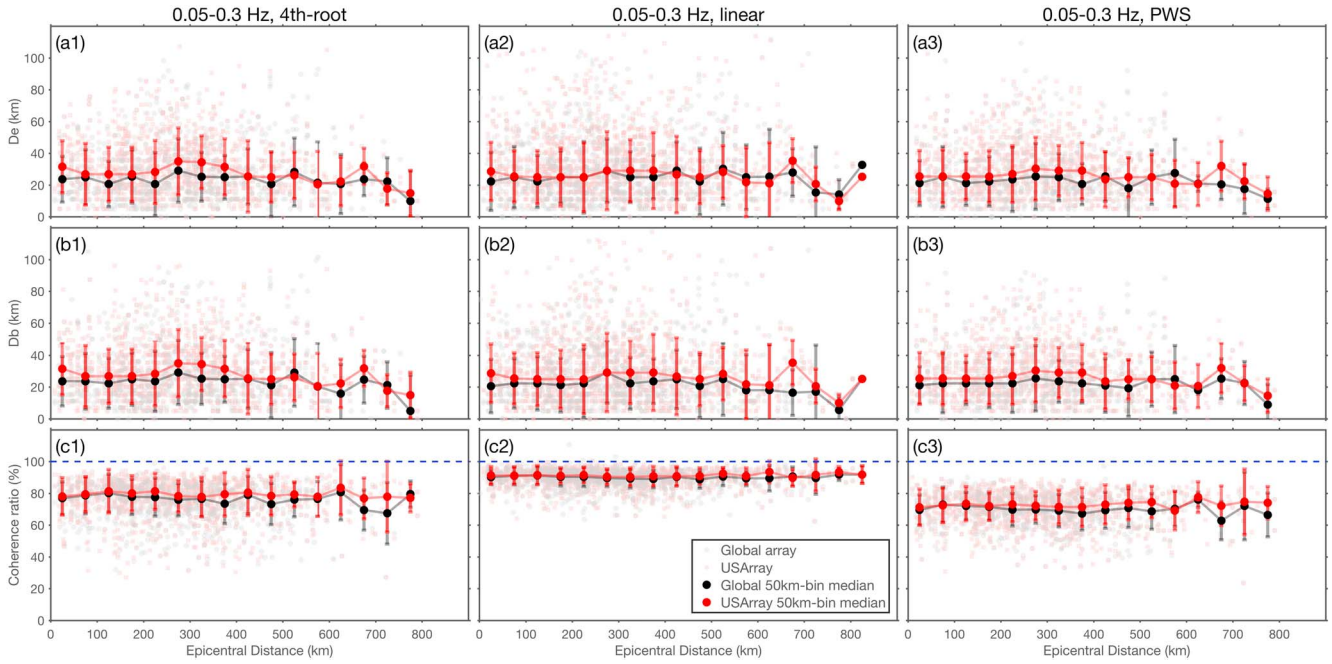

Figure 8. Deviation distances from epicenters (De) and backprojection peak energy loci (Db), and coherence ratios with linear, fourth-root stacking, and phase-weighted stacking (0.05–0.3 Hz), as a function of epicentral distance. Each dot shows one event pair measurement for global (transparent black) and regional (transparent red) arrays. Solid dots show the measurement median of every 50 km bin for both arrays, which are plotted at the center of each distance bin. One standard deviation (SD) of the measurements of each distance bin is shown as the vertical error bar.

control criteria for this particular event due to its complex waveforms causing misalignments and low average cross-correlation coefficients compared to the rest of the global array. Both global and regional array data can clearly resolve the event, as shown by the first 20 s integrated images with either linear or nonlinear stacking, although the global array has higher spatial resolution and *N*th root stacking leads to more compact energy burst images (Figures 3b–3g and 4b–4g). High-frequency backprojection has higher spatial resolution with more compact images compared to low-frequency backprojection (Figures 3b–3g and 4b–4g). This is expected as the resolving power scales inversely with the dominant period of the band-pass frequency band (Fan & Shearer, 2015). Here the 80% energy contours in Figures 4b–4g are about twice smaller than those in Figures 3b–3g, which is comparable to the ratio of dominant periods (~6 s for low frequency, and ~3 s for high frequency) in the filtered seismograms (Figures 3a and4a). When integrating just the first 10 s at 0.05–0.3 Hz and the first 5 s at 0.3–1 Hz for both global and regional arrays, the peak energy locations are centered on the epicenter, showing the effectiveness of the cross-correlation approach in neutralizing 3-D velocity effects. The peak energy locations of the integrated images may deviate from the epicenters, suggesting finite rupture extent/duration of the M_w6.5 earthquake, sourceside scattering effects, or depth phase effects (Figures 3b–3g and 4b–4g). Depth phases (*pP* and *sP*) can cause longer apparent durations (Fan & Shearer, 2015). But when using long stacking windows and data from the global array, the depth phases do not bias the locations very much as shown in Figure S1 for the 2 December 2005 M_w6.5 earthquake.

For giant earthquakes like the 2004 Sumatra-Andaman earthquake, rupture lengths can exceed a thousand kilometers. This large spatial extent may cause the initial time calibrations at the epicenter region to fail at later/further rupture stages when the rays are crossing different parts of the underlying heterogenous 3-D velocity structure (Figure 2c) (Ishii et al., 2005, 2007). The time corrections may also be flawed if the earthquake contains subevents with different focal mechanisms, such that both landward and seaward faults are activated, where the Green's functions change rapidly across the trench. For these cases, the imaged rupture may be shifted to erroneous locations/time, or artifacts may be present, which could be difficult to distinguish from the true rupture features. To assess the robustness and uncertainties of hypocenter-calibrated backprojection

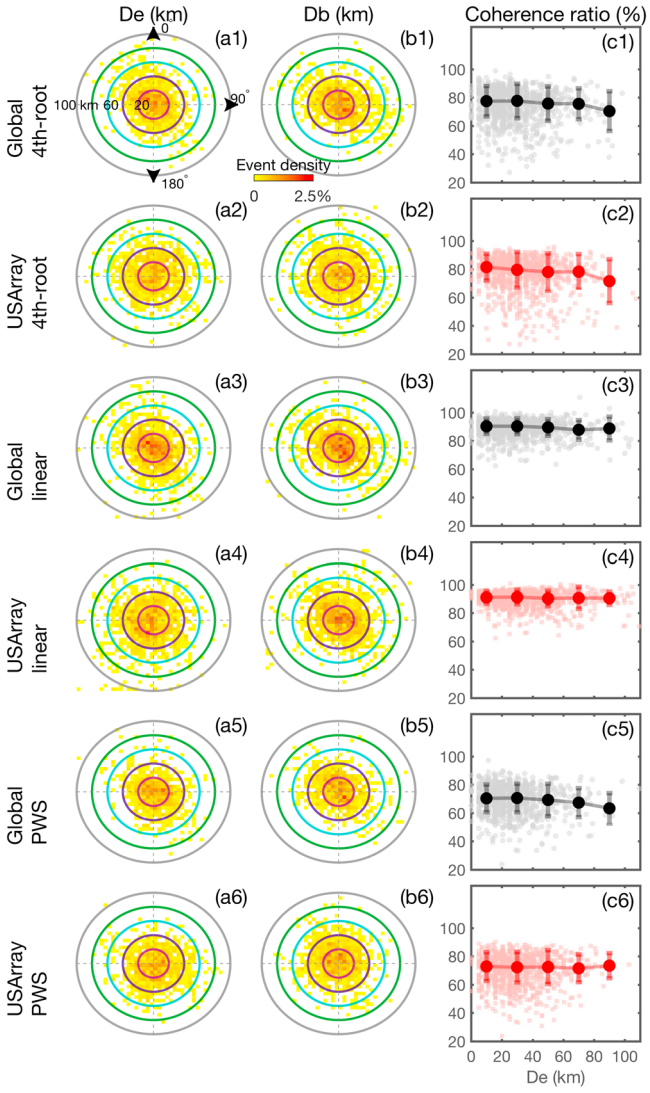

Figure 9. Deviation distance density distribution and coherence ratio versus De with linear, fourth-root stacking, and phase-weighted stacking (0.05–0.3 Hz). (a) De density distribution, normalized with total event pair number, with epicenters located in the center for global stations and USArray with linear and nonlinear stacking approaches. (b) Db density distribution, normalized with total event pair number, with epicenters located in the center for global stations and USArray with linear and nonlinear stacking approaches. (c) Coherence ratio versus De obtained for global stations and USArray with linear and nonlinear stacking approaches. Each dot shows one event pair measurement for global (transparent black) and regional (transparent red) arrays. Solid dots show the measurement median of every 20 km bin for both arrays, which are plotted at the center of each distance bin. One standard deviation (SD) of the measurements of each distance bin is shown as the vertical error bar. USArray is loosely defined as stations within the azimuthal range from 0° to 90°.

across extended regions, we perform backprojection of *M*6 earthquakes with time calibrations obtained from waveform alignments from other earthquakes (Figures 2c and 2d). The empirical time calibrations are derived from waveform cross correlation for each earthquake individually and separately at two frequency bands, then the time calibrations are applied to other earthquakes to obtain backprojection images. For a given earthquake, *P* wave polarity-flip artifacts are unlikely to be present due to our strict data selection criteria. For any of the *M*6 earthquakes, only stations that recorded both the imaged and the calibration earthquakes are used, which often results in fewer useable stations. For example, USArray moved eastward during its deployment, which reduces the shared stations for events occurring at different times even when they are spatially close.

As described above, we apply the time calibration obtained from the 17 August 2011 M_w6.2 normal-faulting earthquake (Event 33) to the shared stations to image the 2 December 2005 M_w6.5 reverse-faulting earthquake (Event 4, Figure 1). These two events occurred 6 years apart, reducing the number of common stations (Figures 5a and 6a). The waveforms of the reverse-faulting earthquake (imaged earthquake) are less well aligned when using the reference time calibrations (Figures 5a and 6a). Interestingly, the misalignments in the first few seconds do not defocus the images but shift the energy bursts instead (Figures 5b–5g and 6b–6g). These spatial shifts can be measured from either the epicenter or the self-aligned backprojection energy locations imaged from only the stations shared in common (Figure 2d), which can be defined as the deviation distance from the epicenter (De) and the deviation distance from the peak location of the self-aligned backprojection image (Db). The deviation distances are measured based on the first 20 s integrated images. In addition, the misalignment will reduce the strength of the stacks, causing incoherence. Because different events have different magnitudes, different focal mechanisms, and may have been recorded with different stations, we use coherence ratios to quantify the incoherence introduced by the misalignment. Coherence ratios are calculated from the 20 s integrated energy images, as the ratio between the peak power in the reference-aligned and self-aligned backprojection images, using identical traces but different alignments.

3. Results

For every *M*6 earthquake, we apply its time calibration to backproject all the other events that were recorded by more than 20 common stations with high-quality data. As an example, Figure 7a shows 11 of 29 events that were imaged with 0.05–0.3 Hz *P* waves with time calibrations obtained from Event 33 (*N*th root stacking). Despite different focal mechanisms between Event 33 and the imaged events, earthquakes with all types of focal mechanisms (reverse, normal, and strike slip) were imaged clearly at both sides of the trench, hosted by faults at the plate interface, the outer rise, and the upper plate, extending across the whole study region (Figure 7a). Most of the reference-alignment-imaged events are close to their epicenters with maximum De of 63 km (Figure 7b) with no preferred direction or clear trend in the deviations (Figure 7d). The imaged events retain high coherence ratios (~80%) over the entire region without noticeable spatial decay when they move away from Event 33 (Figure 7c).

In most backprojection studies, defocused images lacking a clear peak are considered likely artifacts and are not interpreted due to their large uncertainties. Although ruptures occurring simultaneously at multiple parts of the fault have been reported in both dynamic simulations and a few observational cases

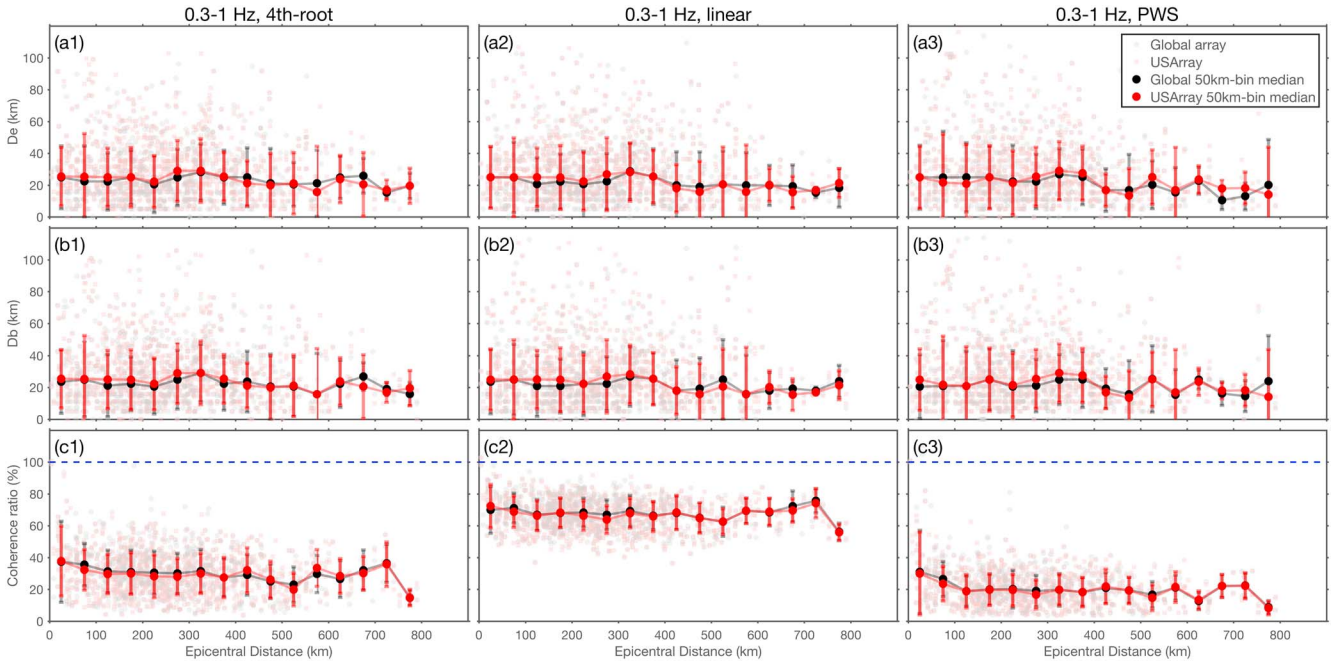

Figure 10. Deviation distances from epicenters (De) and backprojection peak energy loci (Db), and coherence ratios with linear and fourth-root stacking (0.3–1 Hz), as a function of epicentral distance. Legends are similar to Figure 8.

(e.g., Dunham & Archuleta, 2004; Melgar et al., 2016; Oglesby et al., 2004), we conservatively restrict our analysis to well-focused backprojection images, assuming the *M*6 earthquakes have simple rupture kinematics. We visually inspect the backprojection images and remove the defocused ones (more than one peak or a peak too close to the grid edges) to avoid potential artifacts, with an example shown in Figure S2. The inspections are performed for *N*th root stacking results at two frequency bands, respectively, and the same selections are applied to linear stacking and phase-weighted stacking for comparison. Global and USArray results are inspected separately.

Before any event pair removal, there were 1,482 and 1,640 event pairs for low- and high-frequency bands (39 events are investigated for 0.05–0.3 Hz, and 40 events are investigated for 0.3–1 Hz). There were 218 and 366 event pairs that shared less than 20 stations in common for the global array at the two frequency bands (0.05–0.3 Hz and 0.3–1 Hz), and 406 and 494 event pairs for USArray. After automatically removing these event pairs, an additional 257 and 300 event pairs were removed from the global array backprojection images at the two frequency bands following visual inspections (0.05–0.3 Hz and 0.3–1 Hz), and 60 and 150 for USArray. We then examine the spatial patterns of De, Db, and coherence ratio with all the event pairs that passed visual inspections, the measurements include 1,007 and 974 event pairs for the global array at the two frequency bands (0.05–0.3 Hz and 0.3–1 Hz), and 1,016 and 996 pairs for USArray. Summaries of the results are shown in Figures 8 to 13 and Table 1. Results without visual inspections are shown in Figures S3 and S4 (taking *N*th root and linear stacking as examples).

The deviation distances from the epicenters (De) show similar spatial patterns for both the global array and USArray in the two frequency bands (Figures 8–13). De does not significantly increase with epicentral distance between the calibration events and the imaged events, while De also does not converge to zero when the separation distance approaches zero (Figures 8a and 10a). For example, 78.4% of De are below 40 km for the global array with fourth-root stacking at 0.05–0.3 Hz (Figure 8a). The median of De remains at ~25 km even when the event pairs are 700 km apart. De medians for USArray are slightly larger than those from the global array for both frequency bands, but they do not exceed 40 km. Different stacking approaches produce similar spatial patterns for De at both frequency bands respectively, although the imaged energy bursts often have larger spatial extents for linear stacking (Figures 5, 6, 8a, and 10a). De medians share very similar spatial

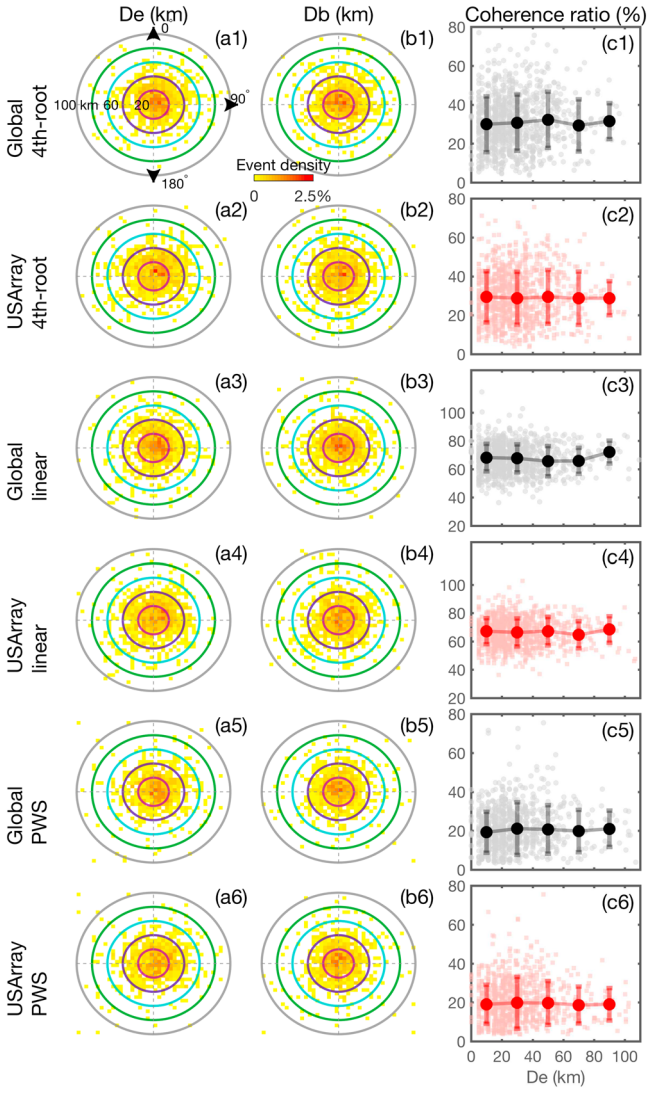

Figure 11. Deviation distance density distribution and coherence ratios versus De with linear, fourth-root stacking, and phase-weighted stacking (0.3–1 Hz). Legends are similar to Figure 9.

patterns for both the low- and high-frequency bands (Figures 8a and 10a). No preferred deviation directions can be identified in both USArray and the global array at the two frequency bands (Figures 9a and 11a). The deviation distances from the peak locations of self-aligned backprojection images (Db) are similar to those of De for all the event pairs (Figures 8–11).

Coherence ratios decay significantly just kilometers away from the calibration *M*6 epicenters and then remain stable up to ~700 km away without any obvious drop (Figures 8c and 10c). For example, the coherence ratio drops to ~80% 20 km away from the epicenters and remains at ~80% up to ~700 km with 88.1% of event pairs above 60% for the global array with fourth-root stacking at 0.05–0.3 Hz (Figure 8c). USArray has higher coherence ratios compared to the global array at both frequency bands, and linear stacking has higher coherence ratios compared to nonlinear stacking at both frequency bands. As might be expected, in all cases the low-frequency band (0.05–0.3 Hz) has higher coherence ratios compared to the high-frequency band (0.3–1 Hz). The coherence ratio is a weak function of De, showing no obvious decay when De increases (Figures 9c and 11c).

To further understand the statistics of De, Db, and the coherence ratio, we estimate the means, medians, and standard deviations of the parameters shown in Table 1. In addition, we model the probability distribution of the parameters by fitting generalized extreme value (GEV) distributions for the coherence ratio (McFadden, 1978) (Figures 12 and 13). The GEV distribution is data driven and can model the smallest or largest value among a large set of independent, identically distributed random values representing observations. The probability density function (PDF, ρ) with x as support for the GEV distribution is decided by location parameter μ, scale parameter σ, and shape parameter κ:

$$\rho(x) = \frac{1}{\sigma} t(x)^{\kappa+1} e^{-t(x)} \quad (1)$$

where $t(x) = e^{-(x-\mu)/\sigma}$ when $\kappa = 0$, or $t(x) = (1 + \kappa\frac{(x-\mu)}{\sigma})^{-1/\kappa}$ when $\kappa \neq 0$. The modeled distribution parameters are listed in Table 1. The statistics confirm that the location uncertainties for De, Db are small (median $\leq$ 30), and the coherence ratios are within narrow bands (standard deviation $\leq$ 20%).

To understand the nonzero convergence of De and Db, we perform backprojection for all the selected event pairs with various stacking windows, including 4 s for the high-frequency band and 10 s for both frequency bands (taking linear and *N*th root as examples, Figures S5–S7). These shorter stacking windows might help to exclude depth phase effects and sourceside scattering. On the other hand, shorter stacking windows can degrade the robustness of the backprojection images and cause larger scatter in the measurements, which is particularly the case for the 4 s window (0.3–1 Hz) when linear stacking is implemented for the global array (Figure S6). The results suggest that De, Db and the coherence ratio generally share similar spatial patterns with different stacking windows (Figures 8,10, and S5–7). With shorter stacking windows, De medians for the global array are slightly larger than those from USArray. For event pairs within 100 km, Figure 14 shows comparisons of De, Db, and coherence ratio using different stacking windows for the two frequency bands with *N*th root stacking. The measurements show no clear spatial trends for De, Db and coherence ratio (Figure 14). Coherence ratios for the high-frequency band suggest an apparent decay up to 30 km. But the limited samples of the measurements and the large standard deviations make the decay relationship unclear (Figure 14f).

4. Discussion

Backprojection imaging has similarities to the earthquake location problem. One of the leading sources of errors in global earthquake locations is the biasing effect of unknown or incorrect 3-D velocity structure

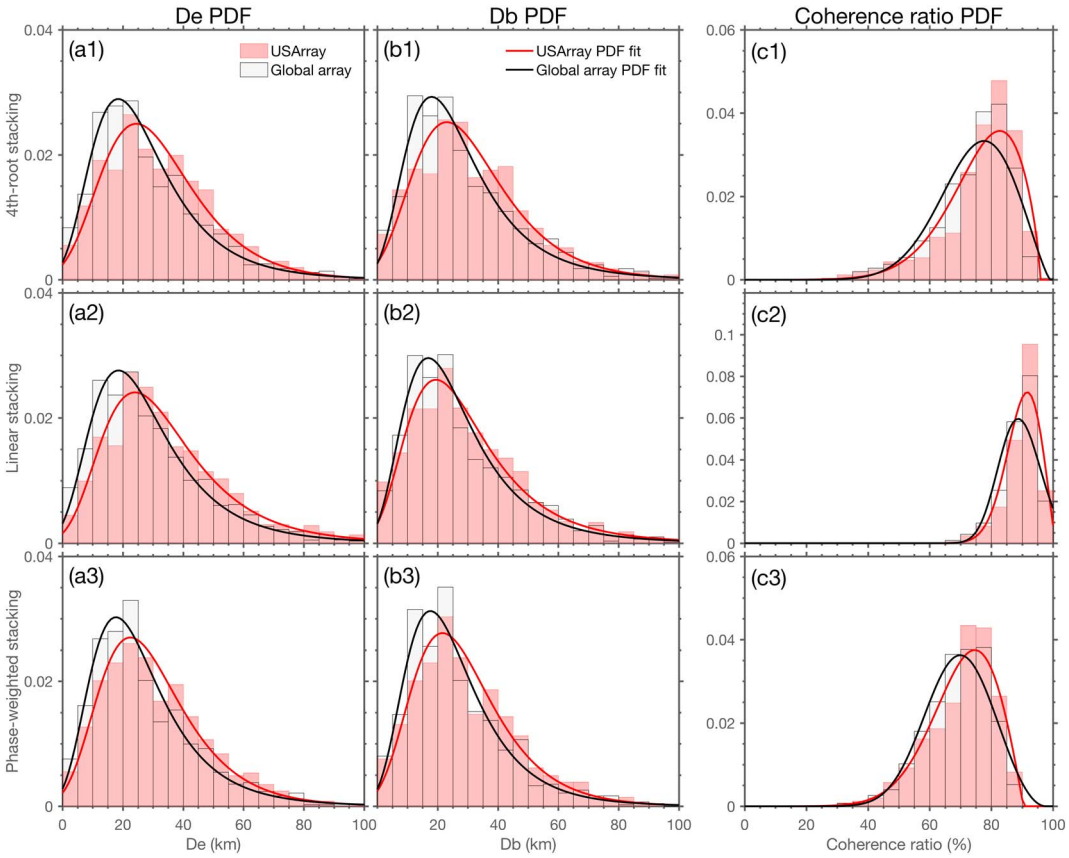

Figure 12. Distributions of De, Db, and coherence ratios at 0.05–0.3 Hz. The fitted probability density functions (PDF) follow generalized extreme value (GEV) distributions, which parameters are listed in Table 1.

(e.g., Thurber, 1983, 1985). In the absence of improvements to 3-D velocity models, empirical approaches can be used to improve relative earthquake locations within localized regions by accounting for the correlated travel time residuals from the region to more distance stations (Douglas, 1967; Hauksson & Shearer, 2005; Jordan & Sverdrup, 1981; Lin, 2013; Lin & Shearer, 2005; Lin et al., 2007; Matoza et al., 2013; Trugman & Shearer, 2017; Shearer et al., 2005; Waldhauser & Ellsworth, 2000; Waldhauser & Schaff, 2008). A particularly simple approach is the master-event technique, in which travel time residuals for a single reference event are used as time corrections to relocate other nearby events. This is analogous to backprojection imaging using the time corrections derived from the hypocenter to better locate energy bursts at other parts of the rupture. A key question for both problems is quantifying how close the reference event needs to be to the target event in order to improve the location, which is related to the spatial coherence of travel time residuals due to 3-D structure as a function of event separation distance.

One way to assess uncertainties in relative earthquake locations due to influences of near-source 3-D velocity structure is to "relocate" stations, which takes advantage of source-receiver reciprocity and the fact that the true station locations are precisely known (Buehler & Shearer, 2016; Shearer, 2001). The station relocation results show that the station mislocation vectors change rapidly over short distances (Buehler & Shearer, 2016). For example, relocations of the USArray stations show that mislocation vectors do not converge to zero even for very close station pairs (Buehler & Shearer, 2016). Such biases are very similar to what we observe for De (Figure 8–11). On average, De does not converge to zero even when event pairs are within 20 km (Figure 8–11), suggesting that strong near-source 3-D velocity variations are a leading source of location error and are approximately random in their effects. Shallow events likely occur in an environment where strong small-scale heterogeneity is present, at scales comparable to the ~6 to ~50 km wavelengths of the *P* waves

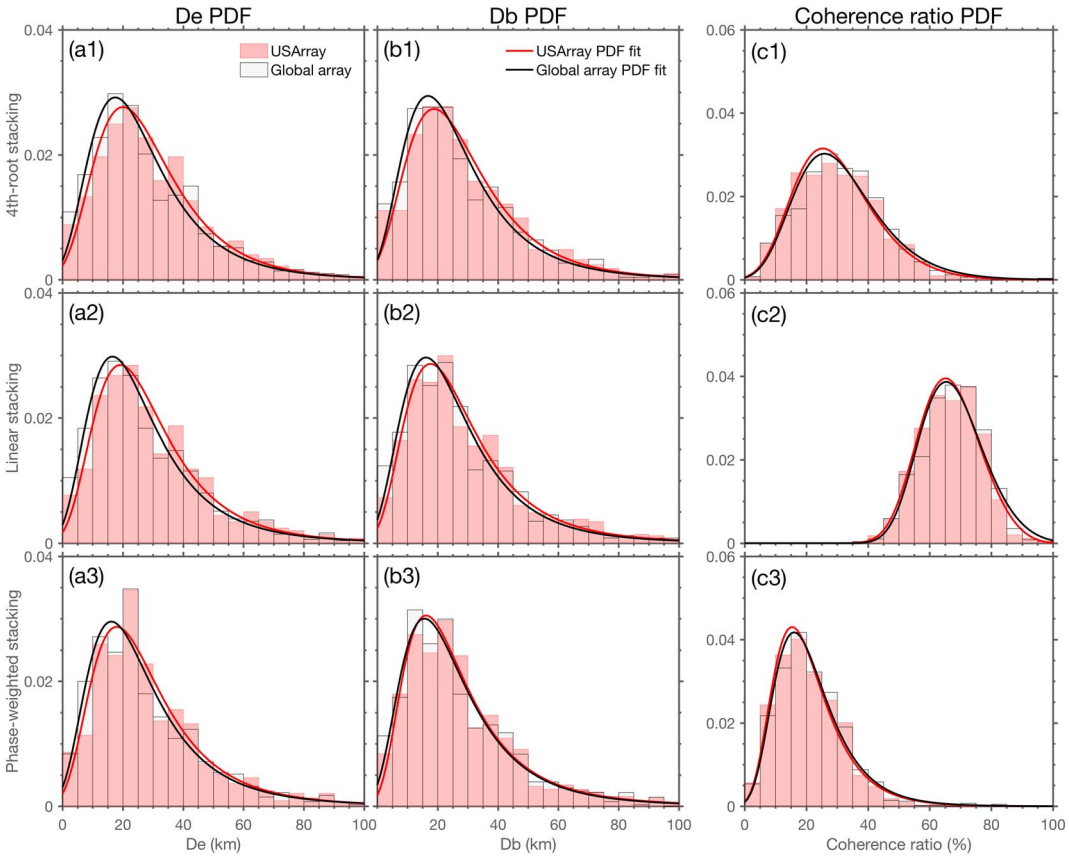

Figure 13. Distributions of De, Db, and coherence ratios at 0.3–1 Hz. The fitted probability density functions (PDF) follow generalized extreme value (GEV) distributions, whose parameters are listed in Table 1.

used for backprojection (~0.1–1 Hz) (Flatté & Wu, 1988; Gudmundsson et al., 1990). This heterogeneity can produce strong near-source scattering, distorting the first arrival of shallow events, and introducing some randomness into the waveform alignment (Flatté & Wu, 1988; Gudmundsson et al., 1990).

Another potential source for the nonzero convergence of De at small separation distance involves the cross-correlation method itself, for which window length, frequency band, and required signal-to-noise ratio are empirically chosen and can introduce random timing uncertainties of ~0.1 s (Huang et al., 2016; VanDecar & Crosson, 1990). The 3-D velocity heterogeneity and random errors from cross correlation make it difficult to use calibration events to improve backprojection images because the events would need to span the entire region at a spacing of 10 km or less (we have not resolved exactly how close they need to be). However, the good news is that the travel time perturbations are largely random and uncorrelated at different locations, such that the average deviations (De) remain stable around 25 km over the whole study region (~700 km) without obvious fluctuations. The relatively small De implies that the standard approach of producing hypocenter-calibrated backprojection images is fairly robust and can be used to map very large ruptures.

The observed spatial patterns of De also suggest that low-frequency backprojection can provide subevent location accuracy comparable to high-frequency backprojection despite the broader imaging kernels at low frequencies (Figures 8 and 10). Deviations in the peak energy locations are mostly introduced by local heterogeneities in the source regions, which randomize the time calibrations for both frequency bands in similar ways. In general, the global array has higher resolution than USArray because of its superior azimuthal coverage. However, the mislocation vectors, De, from USArray observations do not have a preferred azimuthal distribution, suggesting the biases caused by 3-D structure do not relate to array geometry or local tectonics in simple ways (Figures 9 and 11). Nonlinear stacking yields more compact backprojection images (Figures 3–6)

Table 1
Statistics of De, Db, and the Coherence Ratio (Mean, Median, and Standard Deviation Units Are Kilometers for De and Db and Percent for Coherence Ratio)

Array, method	Mean	Median	Standard deviation	κ	σ	μ
			De (0.05–0.3 Hz)			
Global, fourth root	27.9	24.9	17.7	0.1	12.8	19.5
USArray, fourth root	32.1	29.8	18.0	−0.0	14.7	24.0
Global, linear	28.9	25.0	18.9	0.1	13.4	19.8
USArray, linear	34.7	30.3	21.0	0.1	15.3	24.9
Global, PWS	26.9	22.3	17.1	0.1	12.2	18.7
USArray, PWS	30.4	26.9	17.2	−0.0	13.6	22.5
			Db (0.05–0.3 Hz)			
Global, fourth root	28.0	24.9	18.0	0.1	12.6	19.3
USArray, fourth root	31.4	29.0	18.4	−0.0	14.6	23.0
Global, linear	27.4	22.3	18.5	0.1	12.5	18.4
USArray, linear	30.4	25.5	20.4	0.1	14.2	20.8
Global, PWS	26.1	22.3	16.4	0.1	11.8	18.4
USArray, PWS	29.2	25.5	16.7	−0.0	13.3	21.6
			Coherence Ratio (0.05–0.3 Hz)			
Global, fourth root	74.4	77.0	11.6	−0.4	12.4	71.2
USArray, fourth root	76.5	79.5	12.1	−0.6	12.8	74.0
Global, linear	89.0	90.1	5.8	−0.3	6.4	86.8
USArray, linear	89.9	91.1	5.4	−0.5	5.8	88.5
Global, PWS	69.1	70.2	10.2	−0.3	10.8	65.7
USArray, PWS	70.4	72.5	10.7	−0.5	11.5	67.8
			De (0.3–1 Hz)			
Global, fourth root	27.6	24.9	18.2	0.1	12.7	18.8
USArray, fourth root	29.7	26.8	18.3	0.1	13.3	21.0
Global, linear	27.5	22.3	18.8	0.1	12.5	18.3
USArray, linear	29.8	25.4	19.0	0.1	13.0	20.6
Global, PWS	27.9	22.3	20.3	0.2	12.6	18.2
USArray, PWS	29.4	24.9	20.4	0.2	12.9	19.8
			Db (0.3–1 Hz)			
Global, fourth root	27.5	22.3	18.7	0.1	12.6	18.4
USArray, fourth root	29.3	25.0	19.4	0.1	13.5	20.0
Global, linear	26.9	22.3	18.9	0.1	12.5	17.8
USArray, linear	29.1	24.9	20.0	0.2	13.0	19.4
Global, PWS	27.2	22.3	20.0	0.2	12.4	17.6
USArray, PWS	28.5	24.9	20.7	0.2	12.3	18.4
			Coherence Ratio (0.3–1 Hz)			
Global, fourth root	31.3	30.4	14.3	−0.1	12.2	25.1
USArray, fourth root	30.1	29.3	13.4	−0.1	11.7	24.2
Global, linear	67.5	67.6	9.9	−0.2	9.7	63.5
USArray, linear	66.5	66.8	9.7	−0.2	9.6	62.8
Global, PWS	21.7	19.8	12.1	0.0	8.8	16.3
USArray, PWS	20.9	19.4	11.7	0.0	8.6	15.7

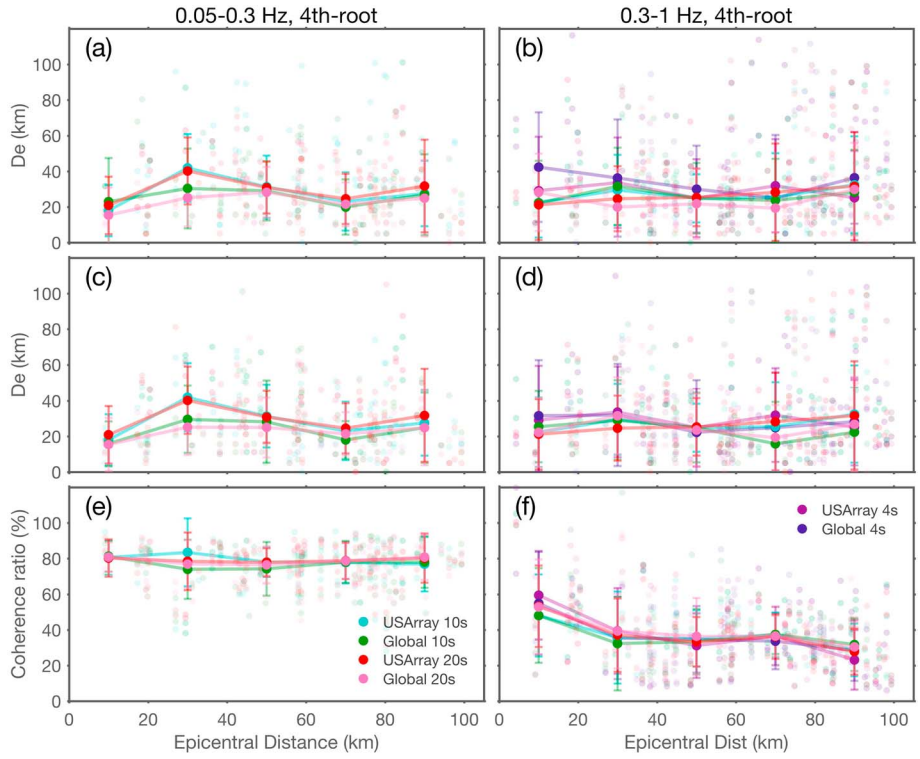

Figure 14. Deviation distances from epicenters (De) and backprojection peak energy loci (Db), and coherence ratios with different stacking window lengths at both frequency bands (fourth-root stacking), as a function of epicentral distance (≤100 km). Solid dots show the measurement median of every 20 km bin for both arrays, which are plotted at the center of each distance bin. One standard deviation (SD) of the measurements in each distance bin is shown as the vertical error bar. The legends are the same as Figure 8.

but does not reduce the mislocation errors. However, it may still improve backprojection images for large earthquakes, because nonlinear stacking equalizes amplitudes and enhances the later signals (Xu et al., 2009).

Another consequence of heterogeneous near-source 3-D velocity structure is the sharp loss of coherence when event pairs are just kilometers apart (Figures 8c and 10c) due to differences in the time calibrations. Coherence ratios remain stable for the whole study region, up to ~700 km between event pairs, indicating that the time calibrations do not vary smoothly and instead have sharp changes caused by random shifts at each event location. This stability suggests that the relative strength between different subevents in backprojection images is likely not biased very much by coherence differences from inaccurate time calibrations. However, low-frequency backprojection is less sensitive to the inaccurate time calibrations, while high-frequency backprojection is more sensitive (Figures 8c and 10c). This hampers efforts to quantitatively evaluate radiation strength between different frequency bands for a given earthquake by backprojection. It is particularly true when nonlinear stacking approaches are employed, which reduces the coherence ratios by more than 50% at 0.3–1 Hz during our experiments (Figures 10c and 13c). The linear stacking approach preserves the coherence ratio strengths much better; for example, the median coherence ratios are ~90% at 0.05–0.3 Hz for both USArray and global stations (Figures 8c and 12c). Coherence ratios obtained with USArray are higher than those with global data, as a result of highly coherent waveforms from regional arrays. Moreover, the coherence ratios do not scale with De (Figures 9c and 11c), suggesting that the inaccurate time calibrations that cause location differences are weakly correlated to the total variance in the time calibrations. An example is shown in Figure 7c, in which the coherence ratios are above ~80% and vary widely from region to region and do not appear to correlate with local tectonics. Some nearby events have quite different coherence ratios, suggesting that near-source shallow 3-D structure controls the process.

Our observations of coherence ratios, De and Db, imply that it is difficult to improve backprojection images with aftershock calibration. Large aftershocks ($M \geq 5.5$) typically sample the main shock fault plane very unevenly, so that for each station, time calibrations derived from aftershocks must be either interpolated

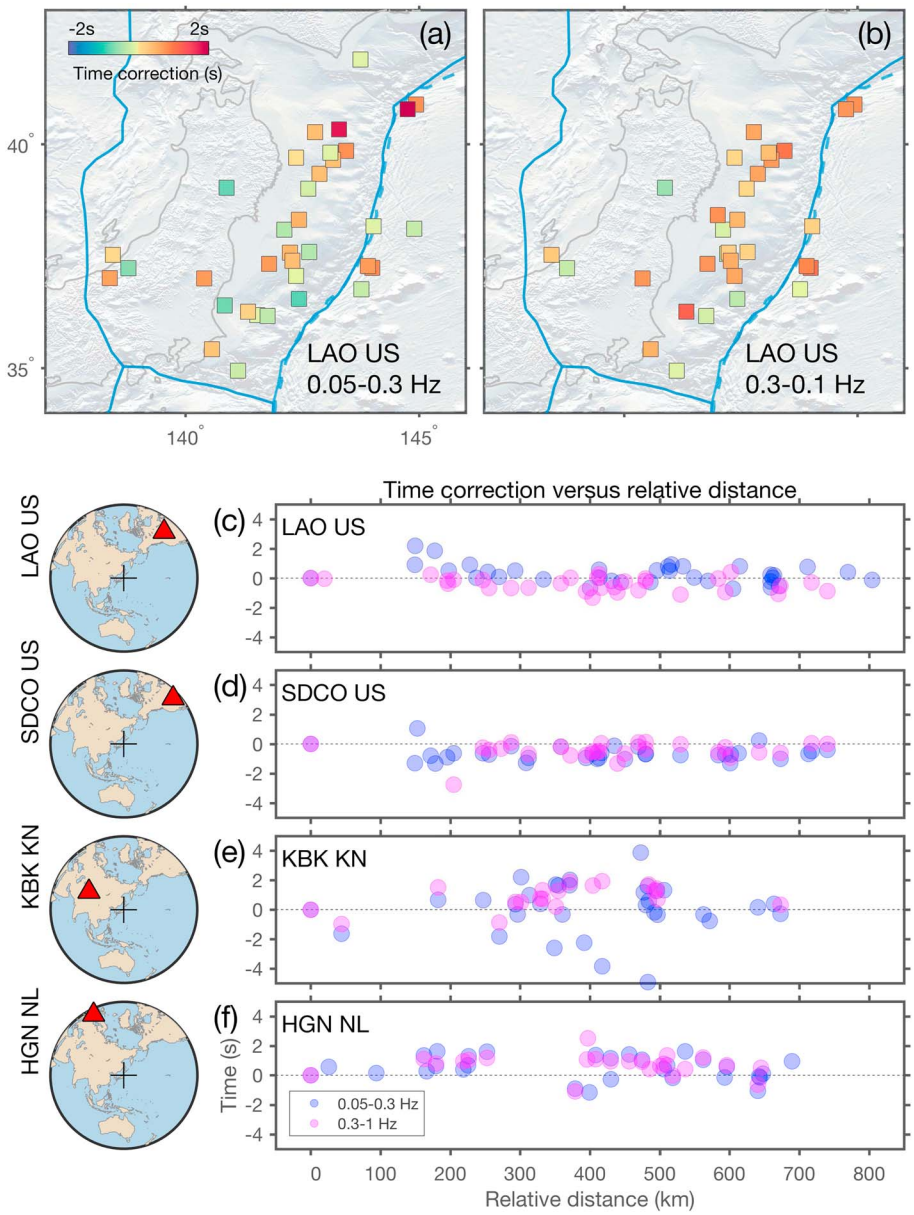

Figure 15. (a and b) Time calibrations for station LAO in two frequency bands and relative time versus relative distance for station (c) LAO, (d) SDCO, (e) KBK, and (f) HGN.

or extrapolated onto all of the hypothetical source locations for the backprojection image. In practice, weighting can also be used to enhance contributions from the higher-quality aftershock records (Ishii et al., 2007). An underlying assumption behind this approach is that the near-source velocity structure is relatively homogenous or varying smoothly. For fine-scale structures, which vary rapidly at shallow depth, such assumptions often cannot be met (e.g., Wang & Zhao, 2005; Zhao et al., 2011), as is suggested by the spatial pattern of De and coherence ratios observed in this study (Figure 8–11).

A related approach to accounting for inaccurate time calibrations in backprojection involves an extra grid station-based time correction (Meng et al., 2016). For a given source grid, this extra time calibration term is $\delta\mathbf{s} \cdot (\mathbf{x_i} - \mathbf{x_0})$, the product of the distance between the grid point ($\mathbf{x_i}$) and the epicenter ($\mathbf{x_0}$) and a slowness correction term $\delta\mathbf{s}$, which is designed to correct to first order for 3-D velocity variation effects between the source grid and the station (Meng et al., 2016). This approach computes a station-specific slowness correction and assumes the correction is valid for the whole rupture region, implying a smooth variation in the time corrections across the source grid. If this is the case, we would expect the aftershock-derived time calibrations

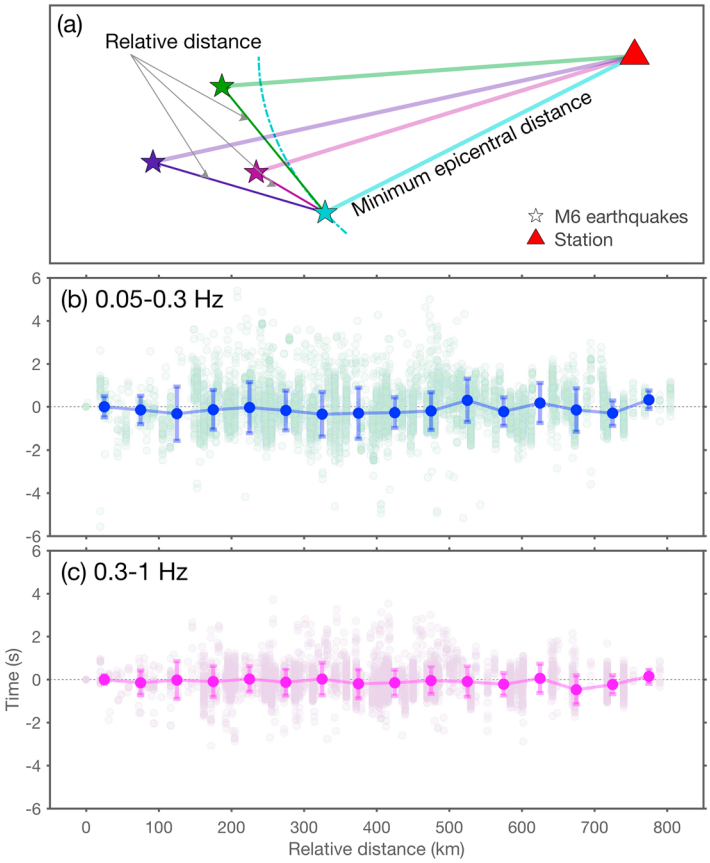

Figure 16. (a) Illustration of relative distances for a given station, and (b and c) relative time versus relative distance for all the stations recording more than 15 events in two frequency bands.

to have smooth and continuous spatial distributions for a given station, but this is not what we have found for the Japan subduction zone. As shown for an example station in Figures 15a and 15b, the spatial distributions of our *M*6-derived calibrations do not vary smoothly or continuously.

Another way to test the slowness correction approach is to examine the relationship between the relative time calibrations and the relative distances to the stations. For a given station, the relative distances are defined as the distances between the closest *M*6 earthquake (minimum epicentral distance) and the other earthquakes, and the relative time calibrations are defined as the differences between the time calibrations of the minimum epicentral distance *M*6 earthquake and other earthquakes (Figure 16a). If the slowness correction hypothesis is correct, then a scaling relationship is expected between the relative distances and relative time calibrations. For four stations at different azimuths, we do not find clear scaling relationships between relative distances and the time calibrations for both frequency bands (Figures 15c–15f). A more comprehensive analysis of all stations recording at least 15 events indicates that the station calibration times generally do not vary smoothly with event distance. This is consistent with the fact that the event mislocation vectors do not vary smoothly with position (e.g., Figure 7d), as gradual location changes would be expected if the calibration times varied smoothly. These observations suggest that the slowness correction approach would not be effective in improving backprojection quality in our study region.

5. Conclusions

We systematically evaluate uncertainties in *P* wave backprojection from velocity model errors by imaging 46 *M*6 earthquakes within the Japan subduction zone. We derive empirical time corrections by cross correlating waveforms of each event and then apply the corrections to other events for backprojection imaging. The analysis quantifies the location and coherence uncertainties introduced by time shifts caused by unknown 3-D velocity variations near the source. Our results show that the standard backprojection method in this

region is robust and should be able to locate subevents with reasonable accuracy, even for ruptures extending ~700 km away from the epicenter used for time calibration. Errors in imaged subevent locations, De, are mostly controlled by near-source fine-scale structures and do not converge to zero even when the event pairs are very close. However, because these near-source variations are largely random and uncorrelated between sources, the biases in the locations do not vary systematically and the location errors average about 20 km from very close to the calibration event to 700 km away. The spatial patterns of De are similar in both frequency bands (0.05–0.3 Hz and 0.3–1 Hz) but suggest that the global array has better spatial resolution than single regional arrays. Similar spatial patterns are observed for coherence ratios, which decay rapidly kilometers away from the calibration *M*6 epicenters while remaining stable up to ~700 km away without a clear decay. On average, regional arrays have higher coherence than the global array, lower frequency backprojection has higher coherence than higher-frequency backprojection, and linear stacking has higher coherence than nonlinear stacking. These observations for the Japan subduction zone reveal no systematic biases that can be correlated to local tectonics or array geometries, suggesting that although it is difficult to improve backprojection images with aftershock calibration, standard backprojection images in the region are reasonably robust with respect to biases from unmodeled 3-D velocity structure. Similar analyses could be used to evaluate backprojection uncertainties in other parts of the world.

Acknowledgments
We would like to thank the Editor Ben-Zion, the Associate Editor Ampuero, and the reviewers for their constructive suggestions, which have led to improvements in our paper. The facilities of IRIS Data Services, and specifically the IRIS Data Management Center, were used for access to waveforms used in this study. IRIS Data Services are funded through the Seismological Facilities for the Advancement of Geoscience and EarthScope (SAGE) Proposal of the National Science Foundation under cooperative agreement EAR-1261681. The earthquake catalog was downloaded from the Global Centroid Moment Tensor (GCMT) project (Ekström et al., 2012). Trench axis data were from Bassett and Watts, (2015a, 2015b). The background bathymetry data were from Sandwell et al. (2014) and Garcia et al. (2014) and were processed with the Generic Mapping Tools (GMT) (Wessel & Smith, 1991; Wessel et al., 2013). This work was supported by National Science Foundation (NSF) [10.13039/100000001] (EAR-1620251) at Scripps Institution of Oceanography, UC San Diego.

References

Allmann, B. P., & Shearer, P. M. (2007). A high-frequency secondary event during the 2004 Parkfield earthquake. *Science*, *318*(5854), 1279–1283.

An, C., & Meng, L. (2016). Application of array backprojection to tsunami prediction and early warning. *Geophysical Research Letters*, *43*, 3677–3685. https://doi.org/10.1002/2016GL068786

Bassett, D., & Watts, A. B. (2015a). Gravity anomalies, crustal structure, and seismicity at subduction zones: 1. Seafloor roughness and subducting relief. *Geochemistry, Geophysics, Geosystems*, *16*, 1508–1540. https: //doi.org/10.1002/2014GC005684

Bassett, D., & Watts, A. B. (2015b). Gravity anomalies, crustal structure, and seismicity at subduction zones: 2. Interrelationships between fore-arc structure and seismogenic behavior. *Geochemistry, Geophysics, Geosystems*, *16*, 1541–1576. https://doi.org/10.1002/2014GC005685

Buehler, J. S., & Shearer, P. M. (2016). Characterizing earthquake location uncertainty in North America using source–receiver reciprocity and USArray. *Bulletin of the Seismological Society of America*, *106*(5), 2395. https://doi.org/10.1785/0120150173

Claerbout, J. F., & Fomel, S. (2008). Image estimation by example: Geophysical soundings image construction: Multidimensional autoregression. Retrieved from: http://sepwww.stanford.edu/sep/prof/, Accessed 4 September 2017.

Douglas, A. (1967). Joint epicentre determination. *Nature*, *215*, 47–48.

Dunham, E. M., & Archuleta, R. J. (2004). Evidence for a supershear transient during the 2002 Denali fault earthquake. *Bulletin of the Seismological Society of America*, *94*(6B), S256–S268. https://doi.org/10.1785/0120040616

Ekström, G., Nettles, M., & Dziewoński, A. (2012). The global CMT project 2004–2010: Centroid-moment tensors for 13,017 earthquakes. *Physics of the Earth and Planetary Interiors*, *200–201*, 1–9. https://doi.org/10.1016/j. pepi.2012.04.002

Fan, W., & Shearer, P. (2015). Detailed rupture imaging of the 25 April 2015 Nepal earthquake using teleseismic P waves. *Geophysical Research Letters*, *42*, 5744–5752. https://doi.org/10.1002/2015GL064587

Fan, W., & Shearer, P. M. (2016a). Local near instantaneously dynamically triggered aftershocks of large earthquakes. *Science*, *353*(6304), 1133–1136. https://doi.org/10.1126/science.aag0013

Fan, W., & Shearer, P. M. (2016b). Fault interactions and triggering during the 10 January 2012 M_w 7.2 Sumatra earthquake. *Geophysical Research Letters*, *43*, 1934–1942. https://doi.org/10.1002/2016GL067785

Fan, W., Shearer, P. M., Ji, C., & Bassett, D. (2016). Multiple branching rupture of the 2009 Tonga-Samoa earthquake. *Journal of Geophysical Research: Solid Earth*, *121*, 5809–5827. https://doi.org/10.1002/2016JB012945

Flatté, S. M., & Wu, R.-S. (1988). Small-scale structure in the lithosphere and asthenosphere deduced from arrival time and amplitude fluctuations at NORSAR. *Journal of Geophysical Research*, *93*(B6), 6601–6614. https://doi.org/10.1029/JB093iB06p06601

Garcia, E. S., Sandwell, D. T., & Smith, W. H. (2014). Retracking Cryosat-2, Envisat and Jason-1 radar altimetry waveforms for improved gravity field recovery. *Geophysical Journal International*, *196*, 1402–1422. https://doi.org/10.1093/gji/ggt469

Grandin, R., Vallée, M., Satriano, C., Lacassin, R., Klinger, Y., Simoes, M., & Bollinger, L. (2015). Rupture process of the M_w = 7.9 2015 Gorkha earthquake (Nepal): Insights into Himalayan megathrust segmentation. *Geophysical Research Letters*, *42*, 8373–8382. https://doi.org/10.1002/2015GL066044

Gudmundsson, O., Davies, J. H., & Clayton, R. W. (1990). Stochastic analysis of global traveltime data: Mantle heterogeneity and random errors in the ISC data. *Geophysical Journal International*, *102*(1), 25–43. https://doi.org/10.1111/j.1365-246x.1990.tb00528.x

Hauksson, E., & Shearer, P. (2005). Southern California hypocenter relocation with waveform cross-correlation, part 1: Results using the double-difference method. *Bulletin of the Seismological Society of America*, *95*(3), 896–903. https://doi.org/10.1785/0120040167

Houser, C., Masters, G., Shearer, P., & Laske, G. (2008). Shear and compressional velocity models of the mantle from cluster analysis of long-period waveforms. *Geophysical Journal International*, *174*, 195–212. https://doi.org/10.1111/j.1365-246x.2008.03763.x

Huang, Y., Ampuero, J.-P., & Kanamori, H. (2014). Slip-weakening models of the 2011 Tohoku-Oki earthquake and constraints on stress drop and fracture energy. *Pure and Applied Geophysics*, *171*(10), 2555–2568. https://doi.org/10.1007/s00024-013-0718-2

Huang, Y., Ampuero, J.-P., & Helmberger, D. V. (2016). The potential for supershear earthquakes in damaged fault zones—Theory and observations. *Earth and Planetary Science Letters*, *433*, 109–115. https: //doi.org/10.1016/j.epsl.2015.10.046

Huang, Y., Meng, L., & Ampuero, J. P. (2012). A dynamic model of the frequency-dependent rupture process of the 2011 Tohoku-Oki earthquake. *Earth, Planets and Space*, *64*(12), 1061–1066. https://doi.org/10.5047/eps.2012.05.011

Ishii, M., Shearer, P. M., Houston, H., & Vidale, J. E. (2005). Extent, duration and speed of the 2004 Sumatra-Andaman earthquake imaged by the Hi-net array. *Nature*, *435*(7044), 933–936.

Ishii, M., Shearer, P. M., Houston, H., & Vidale, J. E. (2007). Teleseismic P wave imaging of the 26 December 2004 Sumatra–Andaman and 28 March 2005 Sumatra earthquake ruptures using the Hi-net array. *Journal of Geophysical Research*, *112*, B11307. https://doi.org/10.1029/2006JB004700

Jordan, T. H., & Sverdrup, K. A. (1981). Teleseismic location techniques and their application to earthquake clusters in the south-central Pacific. *Bulletin of the Seismological Society of America*, *71*(4), 1105–1130.

Kennett, B. L. N., & Engdahl, E. R. (1991). Traveltimes for global earthquake location and phase identification. *Geophysical Journal International*, *105*(2), 429–465. https://doi.org/10.1111/j.1365-246x.1991.tb06724.x

Kiser, E., & Ishii, M. (2011). The 2010 M_w 8.8 Chile earthquake: Triggering on multiple segments and frequency-dependent rupture behavior. *Geophysical Research Letters*, *38*, L07301. https://doi.org/10.1029/ 2011GL047140

Kiser, E., & Ishii, M. (2012). Combining seismic arrays to image the high-frequency characteristics of large earthquakes. *Geophysical Journal International*, *188*(3), 1117–1128. https://doi.org/10.1111/j.1365-246x.2011.05299.x

Komatitsch, D., Liu, Q., Tromp, J., Süss, P., Stidham, C., & Shaw, J. H. (2004). Simulations of ground motion in the Los Angeles basin based upon the spectral-element method. *Bulletin of the Seismological Society of America*, *94*(1), 187–206. https://doi.org/10.1785/0120030077

Koper, K. D., Lay, A. H. T., Ammon, C., & Kanamori, H. (2011). Frequency-dependent rupture process of the 2011 M_w 9.0 Tohoku earthquake: Comparison of short-period *P* wave backprojection images and broadband seismic rupture models. *Earth, Planets, and Space*, *63*(7), 599.

Koper, K. D., Hutko, A. R., Lay, T., & Sufri, O. (2012). Imaging short-period seismic radiation from the 27 February 2010 Chile (M_w 8.8) earthquake by back-projection of *P*, *PP*, and *PKIKP* waves. *Journal of Geophysical Research*, *117*, B02308. https://doi.org/10.1029/2011JB008576

Lin, G. (2013). Three-dimensional seismic velocity structure and precise earthquake relocations in the Salton Trough, southern California. *Bulletin of the Seismological Society of America*, *103*(5), 2694–2708. https://doi.org/10.1785/ 0120120286

Lin, G., & Shearer, P. (2005). Tests of relative earthquake location techniques using synthetic data. *Journal of Geophysical Research*, *110*, B04304. https://doi.org/10.1029/2004JB003380

Lin, G., Shearer, P. M., & Hauksson, E. (2007). Applying a three-dimensional velocity model, waveform cross correlation, and cluster analysis to locate southern California seismicity from 1981 to 2005. *Journal of Geophysical Research*, *112*, B12309. https://doi.org/10.1029/2007JB004986

Mancinelli, N., Shearer, P., & Liu, Q. (2016). Constraints on the heterogeneity spectrum of Earth's upper mantle. *Journal of Geophysical Research: Solid Earth*, *121*, 3703–3721. https://doi.org/10.1002/2015JB012641

Matoza, R. S., Shearer, P. M., Lin, G., Wolfe, C. J., & Okubo, P. G. (2013). Systematic relocation of seismicity on Hawaii island from 1992 to 2009 using waveform cross correlation and cluster analysis. *Journal of Geophysical Research: Solid Earth*, *118*, 2275–2288. https://doi.org/10.1002/jgrb.50189

McFadden, D. (1978). *Modeling the Choice of Residential Location* (Vol. 673, pp. 72–77), Transportation Research Record.

McFadden, P. L., Drummond, B. J., & Kravis, S. (1986). The *N*th–root stack: Theory, applications, and examples. *Geophysics*, *51*(10), 1879–1892. https://doi.org/10.1190/1.1442045

Melgar, D., Fan, W., Riquelme, S., Geng, J., Liang, C., Fuentes, M., … Fielding, E. J. (2016). Slip segmentation and slow rupture to the trench during the 2015, M_w 8.3 Illapel, Chile earthquake. *Geophysical Research Letters*, *43*, 961–966. https://doi.org/10.1002/2015GL067369

Meng, L., Inbal, A., & Ampuero, J.-P. (2011). A window into the complexity of the dynamic rupture of the 2011 M_w 9 Tohoku-Oki earthquake. *Geophysical Research Letters*, *38*, L00G07. https://doi.org/10.1029/ 2011GL048118

Meng, L., Ampuero, J.-P., Luo, Y., Wu, W., & Ni, S. (2012). Mitigating artifacts in back-projection source imaging with implications for frequency-dependent properties of the Tohoku-Oki earthquake. *Earth, Planets and Space*, *64*(12), 1101–1109. https://doi.org/10.5047/eps.2012.05.010

Meng, L., Zhang, A., & Yagi, Y. (2016). Improving back projection imaging with a novel physics-based aftershock calibration approach: A case study of the 2015 Gorkha earthquake. *Geophysical Research Letters*, *43*, 628–636. https://doi.org/10.1002/2015GL067034

Nissen, E., Elliott, J., Sloan, R., Craig, T., Funning, G., & Hutko, A. (2016). Limitations of rupture forecasting exposed by instantaneously triggered earthquake doublet. *Nature Geoscience*, *9*, 330–336. https://doi.org/10.1038/ngeo2653

Oglesby, D. D., Dreger, D. S., Harris, R. A., Ratchkovski, N., & Hansen, R. (2004). Inverse kinematic and forward dynamic models of the 2002 Denali fault earthquake, Alaska. *Bulletin of the Seismological Society of America*, *94*(6B), S214–S233. https://doi.org/10.1785/0120040620

Okuwaki, R., Yagi, Y., & Hirano, S. (2014). Relationship between high-frequency radiation and asperity ruptures, revealed by hybrid back-projection with a non-planar fault model. *Science Reports*, *4*, 7120.

Rost, S., & Thomas, C. (2002). Array seismology: Methods and applications. *Reviews of Geophysics*, *40*(3), 1008. https://doi.org/10.1029/2000RG000100

Sandwell, D. T., Müller, R. D., Smith, W. H. F., Garcia, E., & Francis, R. (2014). New global marine gravity model from Cryosat-2 and Jason-1 reveals buried tectonic structure. *Science*, *346*(6205), 65–67. https://doi.org/10.1126/science.1258213

Satriano, C., Kiraly, E., Bernard, P., & Vilotte, J.-P. (2012). The 2012 M_w 8.6 Sumatra earthquake: Evidence of westward sequential seismic ruptures associated to the reactivation of a N-S ocean fabric. *Geophysical Research Letters*, *39*, L15302. https://doi.org/10.1029/2012GL052387

Schimmel, M., & Paulssen, H. (1997). Noise reduction and detection of weak, coherent signals through phase-weighted stacks. *Geophysical Journal International*, *130*(2), 497–505. https://doi.org/10.1111/j.1365-246x.1997.tb05664.x

Shearer, P., Hauksson, E., & Lin, G. (2005). Southern California hypocenter relocation with waveform cross-correlation, Part 2: Results using source-specific station terms and cluster analysis. *Bulletin of the Seismological Society of America*, *95*(3), 904–915. https://doi.org/10.1785/0120040168

Shearer, P. M. (2001). Improving global seismic event locations using source–receiver reciprocity. *Bulletin of the Seismological Society of America*, *91*(3), 594–603. https://doi.org/10.1785/0120000238

Thurber, C. H. (1983). Earthquake locations and three-dimensional crustal structure in the Coyote Lake area, central California. *Journal of Geophysical Research*, *88*(B10), 8226–8236. https://doi.org/10.1029/JB088iB10p08226

Thurber, C. H. (1985). Nonlinear earthquake location: Theory and examples. *Bulletin of the Seismological Society of America*, *75*(3), 779–790.

Trugman, D. T., & Shearer, P. M. (2017). Growclust: A hierarchical clustering algorithm for relative earthquake relocation, with application to the Spanish Springs and Sheldon, Nevada, earthquake sequences. *Seismological Research Letters*, *88*(2A), 379–391. https://doi.org/10.1785/0220160188

VanDecar, J. C., & Crosson, R. S. (1990). Determination of teleseismic relative phase arrival times using multi-channel cross-correlation and least squares. *Bulletin of the Seismological Society of America*, *80*(1), 150–169.

Waldhauser, F., & Ellsworth, W. L. (2000). A double-difference earthquake location algorithm: Method and application to the northern Hayward fault, California. *Bulletin of the Seismological Society of America*, *90*(6), 1353–1368. https://doi.org/10.1785/0120000006

Waldhauser, F., & Schaff, D. P. (2008). Large-scale relocation of two decades of northern California seismicity using cross-correlation and double-difference methods. *Journal of Geophysical Research*, *113*, B08311. https: //doi.org/10.1029/2007JB005479

Walker, K. T., & Shearer, P. M. (2009). Illuminating the near-sonic rupture velocities of the intracontinental Kokoxili Mw 7.8 and Denali fault Mw 7.9 strike-slip earthquakes with global P wave back projection imaging. *Journal of Geophysical Research*, *114*, B02304. https://doi.org/10.1029/2008JB005738

Walker, K. T., Ishii, M., & Shearer, P. M. (2005). Rupture details of the 28 March 2005 Sumatra Mw 8.6 earthquake imaged with teleseismic P waves. *Geophysical Research Letters*, *32*, l24303. https://doi.org/10.1029/2005GL024395

Wang, D., & Mori, J. (2016). Short-period energy of the 25 April 2015 Mw 7.8 Nepal earthquake determined from backprojection using four arrays in Europe, China, Japan, and Australia. *Bulletin of the Seismological Society of America*, *106*(1), 259–266. https://doi.org/10.1785/0120150236

Wang, D., Mori, J., & Uchide, T. (2012). Supershear rupture on multiple faults for the M_w 8.6 Off Northern Sumatra, Indonesia earthquake of April 11, 2012. *Geophysical Research Letters*, *39*, L21307. https://doi.org/10.1029/2012GL053622

Wang, Z., & Zhao, D. (2005). Seismic imaging of the entire arc of Tohoku and Hokkaido in Japan using P-wave, S-wave and Sp depth-phase data. *Physics of the Earth and Planetary Interiors*, *152*(3), 144–162. https: //doi.org/10.1016/j.pepi.2005.06.010

Wessel, P., & Smith, W. H. (1991). Free software helps map and display data. *Eos Transactions AGU*, *72*(441), 445–446.

Wessel, P., Smith, W. H. F., Scharroo, R., Luis, J., & Wobbe, F. (2013). Generic Mapping Tools: Improved version released. *Eos Transactions AGU*, *94*(45), 409–410. https://doi.org/10.1002/2013EO450001

Xu, Y., Koper, K. D., Sufri, O., Zhu, L., & Hutko, A. R. (2009). Rupture imaging of the M_w 7.9 12 May 2008 Wenchuan earthquake from back projection of teleseismic P waves. *Geochemistry, Geophysics, Geosystems*, *10*, Q04006. https://doi.org/10.1029/2008GC002335

Yagi, Y., & Okuwaki, R. (2015). Integrated seismic source model of the 2015 Gorkha, Nepal, earthquake. *Geophysical Research Letters*, *42*, 6229–6235. https://doi.org/10.1002/2015GL064995

Yagi, Y., Nakao, A., & Kasahara, A. (2012). Smooth and rapid slip near the Japan trench during the 2011 Tohoku-oki earthquake revealed by a hybrid back-projection method. *Earth and Planetary Science Letters*, *355–356*, 94–101. https://doi.org/10.1016/j.epsl.2012.08.018

Zhang, H., van der Lee, S., & Ge, Z. (2016). Multiarray rupture imaging of the devastating 2015 Gorkha, Nepal, earthquake sequence. *Geophysical Research Letters*, *43*, 584–591. https://doi.org/10.1002/2015GL066657

Zhao, D., Huang, Z., Umino, N., Hasegawa, A., & Kanamori, H. (2011). Structural heterogeneity in the megathrust zone and mechanism of the 2011 Tohoku-oki earthquake (Mw 9.0). *Geophysical Research Letters*, *38*, L17308. https://doi.org/10.1029/2011GL048408